Electron Beam Induced Current Detection of Sub-Surface Two-Dimensional Charge Reservoir

A Thesis

Submitted to the Faculty

of

Drexel University

by

Eric G. Myers

in partial fulfillment of the

requirements for the degree

of

Master of Science in Electrical Engineering

April 2008

Dedications

I would like to dedicate this thesis to my fiancé Vernika Neal, my parents, and my siblings for all of their love and support.

Acknowledgements

I would like to thank Dr. Bahram Nabet for his guidance and support in completing this thesis study. With my unusual off-campus schedule accommodations, to understanding my level of commitment to family life, I appreciate all of his, as well as the entire Photonics team's, efforts in giving me the needed direction to follow through.

Many thanks go out to Dr. Jonathan Spanier and his Materials-Science Engineering (MSE) group for making available the laboratorial equipment and their support, and to Eric Gallo for taking what little time he had available to provide input and direction in completing many laboratory tasks. I would also like to thank our collaborators at CNR-IMM in Italy, in the fabrication and electrical characterization of the 2-DHG devices discussed in this thesis.

Most importantly, I would like to thank my family and friends for standing by me through all my college endeavors. Thank you for believing in me and never doubting I would achieve my goals in life; thank you for supporting me when it was needed and pushing me when it was necessary. For this, I am forever indebted.

Table of Contents

List of Tables

List of Figures

Abstract

Electron Beam Induced Current Detection of Sub-Surface
Two-Dimensional Charge Reservoir
Eric G. Myers
Supervisor: Bahram Nabet, PhD

In conjunction with metal-semiconductor-metal heterostructure (HMSM) devices, the electron beam induced current (EBIC) detection method is ideal in two-dimensional sheet charge detection. Using a delta modulation-doped heterostructure, a scan-line plot comparison to its undoped structural equivalent exposes the electrical effects of the sheet charge existence. While electrically biasing both heterostructure types, each were placed in an SEM chamber and electrode-to-electrode scan-line plots were taken at different biasing levels. Based on experimental results, dark currents for the delta modulation-doped device are detrimental to its EBIC signal-to-noise ratio but its electron-hole pair collection rate is more effective in EBIC signaling than its undoped counterpart at higher biasing levels. Bypassing the charge transport limitation of a saturated group drift velocity in the active region, charge carriers are swept to the highly conductive two-dimensional sheet charge in the doped structure resulting in higher EBIC signaling; the sheet charge shields the active region from the drift-current limitations by modifying the carrier transport path within the active region. Supported by experimental EBIC characterization data, biased delta modulation-doped HMSM device simulations predicted the presence of the two-dimensional sheet charge would effectively simulate smaller finger-gapped devices but without sacrificing its active region volume. Improvements in electron beam control, most notably beam depth within a sample, can

aid in the development of a non-destructive EBIC method to determine sheet charge uniformity; an added feature to the established device failure and defect analysis EBIC techniques used today. Theoretical electrical dissimilarities with modulation-doped and undoped in-plane Schottky contact devices are discussed to support the EBIC method and its application; the advantages and/or disadvantages of using degenerate devices of this type in substitution of its undoped structural equivalent are demonstrated.

1. Background in Electron Detection

Electron detectors are used in many applications, most notably in scanning electron microscopy (SEM) and electron beam tomography (EBT). Types of electron detectors used include the following:

- Cathodoluminescence (CL)
- Sample current
- In-lens
- Backscatter
- Secondary
- X-Ray

Each detector type has its characteristic strengths not to mention its weaknesses. Depending on the solid-state device structure and its building material, the ability to detect electrons is greatly affected. In this study, the primary focus is the degenerate device structure where the conduction band electron doping concentration of a host semiconductor is comparable to a metal; its relative differences to non-degenerate device structures based on the cathodoluminescence process are also discussed.

1.1. Electron Detectors

The cathodoluminescence electron detector is used to determine electrical properties of a sample and is sensitive to the optical photons emitted by various materials under charged beam excitation. Based on the cathodoluminescence process, electron-

hole pairs are generated through electron irradiation; a photon is generated upon recombination and is detected. A sample current detector is a sensitive ammeter with fast response time that measures the current passing from the sample stage to ground; total current is a function of the backscattered, secondary, and Auger electron yield. In-lens electron detectors are suitable as particle beam monitors as well as on-axis imaging detectors; its secondary electron detection efficiency is relatively high near the electron beam axis within an SEM chamber.

A scintillator works by converting X-ray energy into visible light. The resulting photon produces excited ions that return to their ground state by transitions involving electrons from a higher energy level to a lower level. The wavelength corresponding to the absorption edge is always less than wavelengths of fluorescence lines. Absorption edges occur at wavelengths where the incident photon has enough energy to knock an electron from its orbit. Conversely, the emission of X-radiation wavelengths is identical to emission resulting from excitation by electron bombardment.

X-ray electron detectors are used to determine elemental composition of a sample, and in doing so, uses X-ray absorption. Energetic electrons' interaction upon striking the scintillator material produces photons that are conducted by total internal reflection in the light guide to the photomultiplier; ejection of an electron from an atom results when an X-ray photon is absorbed. Wavelength-dispersive X-ray detectors (WDX) use semiconductors for the detection of X-ray energy. A photo-electron is produced in the semiconductor by the X-ray photon in which a charge pulse is generated. The pulses are proportional to energies of the X-ray and count vs. energy is the output.

Backscatter electron (BSE) detectors include the silicon diode, scintillator and channel plate. The primary component of the Everhart-Thornley detector is a scintillator; photons are emitted when high-energy electrons strike the scintillator. The emitted photons are collected by a light guide and transported to a photomultiplier for detection. Channel plates take advantage of the electron cascading effect to produce a current; the current is used as a signal.

1.2. Electron Detectors Used in Scanning Electron Microscopes

Most scanning electron microscopes employ the Everhart-Thornley detector for good electron-detection efficiency. In contrast to an optical microscope or transmission electron microscope (TEM), there are no true sample images used to generate images with an SEM; images are mapped by the interpolation of the collected electrons by various types of electron detectors, be it backscattered, transmitted or absorbed electron detection. Changing the electron beam's acceleration, spot size, and spot location, may reveal possible changes in the I-V characteristics of a sample in a closed- circuit.

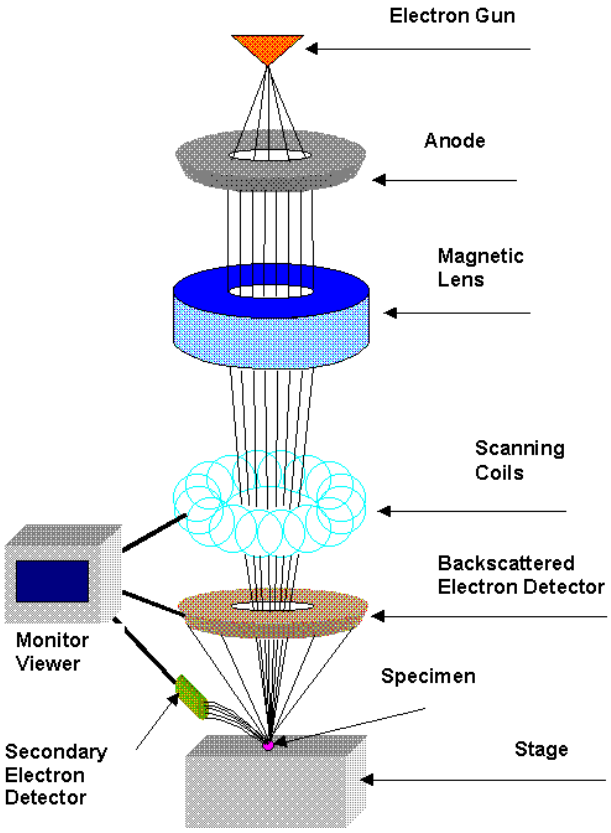

Figure 1-1: Scanning electron microscope pictorial; from [3]

X-ray spectroscopy is the technology behind the development and implementation of the scanning electron microscope (SEM). It is the employment of a radioactive source whose decay process results in X-ray emission. As illustrated in Figure 1-1, high energy electrons are focused into a fine beam with a diameter on the order of a few nanometers and then swept in a raster pattern across the surface of a specimen or sample material for the purpose of gathering electrical, topographical, and compositional characteristics. This high energy beam of electrons bombards the target specimen and generates a secondary beam of X-ray fluorescence; X-ray emission is generated. Elastic and inelastic interactions take place between the electrically accelerated electrons and the specimen

and a variety of radiation emerges [11] [17]. Radiation types include backscattered, secondary and characteristic X-ray. Signal detection and amplification of these radiation types are then mapped and displayed on a cathode ray tube (CRT) or television monitor [17].

Similar to the optical microscope is the transmission electron microscope or TEM. Both the optical and transmission electron microscopes generate images by magnifying true specimen images. Images produced with an SEM are not derived from true imagery; mapping operations that transmit information collected from the SEM chamber are used to generate an image onto the CRT display. Synchronous scans of the specimen and the CRT aide in maintaining geometric relationships between points on the specimen and points on the CRT [17] [11].

Cathode types used in scanning electron microscopes are the tungsten filament, the lanthanum hexaboride, and the field emission gun. The tungsten filament cathode is the most commonly used material for SEM-type cathode-based operations. Electrons are emitted from the heated tip of the cathode toward the anode, otherwise known as thermionic emission. The lanthanum hexaboride cathode is an order of magnitude brighter than tungsten and requires a relatively higher vacuum to operate (10^{-6} to 10^{-7} torr). The field emission gun cathode has a high electric field at the gun tip that is produced by a tunneling process. No heat is required for the field emission gun but it requires a relatively higher vacuum level (10^{-9} torr) [11].

Numerous types of electron detectors are used in SEMs such as the cathodoluminescence, the sample current, the X-ray, the in-lens, the backscatter, and the secondary electron detector. Descriptions of these detectors were previously given. The

cathodoluminescence electron detector is used to determine electrical properties of a sample. In-lens electron detectors are suitable as particle beam monitors as well as on-axis imaging detectors; very high electron detection efficiency. Backscatter electron (BSE) detectors are designed for the most critical high efficiency, high resolution spectroscopic applications. Secondary electron detectors collect information to generate topographic images [35] [17].

Scintillation counting, which is the backbone of energy resolution and the primary action in the Everhart-Thornley detector, is determined by the variation of electrons thermionically emitted by the photocathode. Higher energy resolution allows for distinction between two or more emitted photons with relatively small wavelength differences; i.e. similar emission energies. The scintillator produces visible light which is amplified through a photomultiplier and used to produce an image on a CRT.

During elastic electron collisions, backscatter electrons are produced that gives surface structure and average elemental information. These elastic electrons are deflected due to coulombic interactions with atoms. During inelastic electron collisions, secondary electrons are produced that provides surface structure information. These collisions are also known as inner-shell ionizations. An incident electron knocks a k-shell electron from its energy level thus leaving a vacancy which is eventually filled with an electron from a higher energy state; an X-ray photon is emitted.

Another type of X-ray detector is the energy dispersive X-ray detector (EDX) used in energy dispersive spectroscopy (EDS). An electron beam, typically with energy of 120 keV, strikes the surface of a sample and produces emitted X-rays. The composition of the sample determines the energy of the X-rays emitted. A Lithium

drifted Silicon detector is used in EDX that must be operated at liquid nitrogen temperatures. Electron-holes are created when an X-ray strikes the detector and are attracted to opposite ends of the detector with by a strong electric field and generates a current pulse. Current pulse sizes are dependent on the number of electron-hole pairs created. Logically speaking, current pulses are dependent on the energy of the incoming X-ray, which depends on the composition of the sample. This concludes that an X-ray spectrum acquires information on the elemental composition of the sample or material of a sample that is under examination. Sweeping the electron beam across the entire sample produces an image of each element in the sample [35].

Suitable for extremely low beam energy imaging, from 500 eV to 3 keV, BSE detectors are able to determine the atomic number of a sample along with topographical sample characteristics; they allow the formation of images using the secondary electron signal, which is much more dependent on the sample topography at the point of intersection of the primary beam with the sample. Backscatter electron detectors include the silicon diode, scintillator and channel plate. Scintillators are nothing more than a stripped down version of an E-T detector; secondary electrons are collected and light is produced when the electrons strike the scintillator. Channel plates take advantage of the electron cascading effect to produce a current; the current is used as a signal [35].

A scintillator is a device that absorbs high energy (ionizing) charged particle radiation and responds by fluorescing photons at a characteristic Stokes-shifted wavelength, thus releasing the previously absorbed energy. When positively biased, typically at a 12kV potential, secondary electrons are attracted toward the Faraday cage, which also is normally kept within a potential range 250V to attract secondary electrons.

Secondary electrons enter the cage for subsequent acceleration by the bias of the scintillator. This cage bias deflects secondary electron trajectories over a wider range into the detector. Indirect backscatter electrons strike pole-piece and chamber walls which produce secondary electrons. Although secondary electron detection is highly efficient, these secondary electrons actually represent the backscattered electron signal component [11] [35].

When negatively biased, the scintillator rejects all secondary electrons in the chamber. Only high-energy backscatter electrons that are directed towards the scintillator are detected. The detection of all other backscatter electrons is lost. The photomultiplier tube is an electron tube that produces electrical signals in response to light. The signal is then amplified to produce an output current from small quantities of light [35].

2. Electrical Interface Physics

Depending on the type of material interfacing with the host semiconductor or medium, charge carrier transport through the semiconductor contact interface is greatly affected by the electrical characteristics of the medium. Two types of degenerate semiconductor contacts are discussed; a metal-semiconductor interface and a semiconductor-semiconductor interface. Of major importance in charge carrier transport properties are the doping levels of each interfacing semiconductor involved. As will be explained in section 2.2.2, degenerate semiconductor contacts are more desirable in producing a low-impedance or non-rectifying interface.

2.1. Degenerate Semiconductor-Semiconductor Contacts

A two-dimensional electron gas (2DEG) is typically formed by placing two n-type, iso-type semiconductors, one with a narrow band-gap and the other a wide band-gap, in straddling contact form. Through band bending the conduction band of the narrow band-gap reaches below the equilibrium Fermi level, thus forming a potential well within the narrow band-gap semiconductor where an accumulation layer of electrons is formed (see Figure 2-1). Relative to the narrow band-gapped semiconductor, heavily doping the wide band-gapped semiconductor can further increase the density of the 2DEG. It has been proven that the energy levels in a potential well are quantized, hence the name 2D [27].

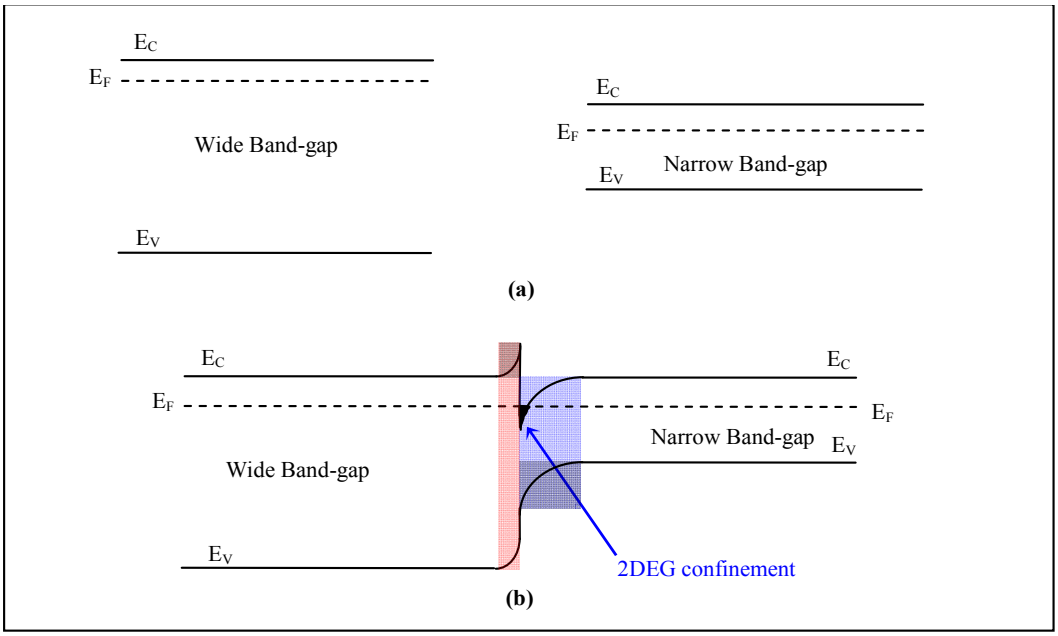

Figure 2-1: N-type wide band-gap and n-type low-doped narrow band-gap semiconductor (a) isolated and (b) in thermal contact

Similar to 2DEG formation, a two-dimensional hole-gas (2DHG) is typically formed in type-I heterojunctions by placing two p-type/iso-type semiconductors, one with a narrow band-gap and the other a wide band-gap, in straddling contact form. Through band bending the valence band of the narrow band-gap reaches above the equilibrium Fermi level, thus forming a potential well within the narrow band-gap semiconductor where an accumulation layer of holes is formed (see Figure 2-2). Relative to the narrow band-gapped semiconductor, heavily doping the wide band-gap semiconductor can further increase the density of the confined charge [27].

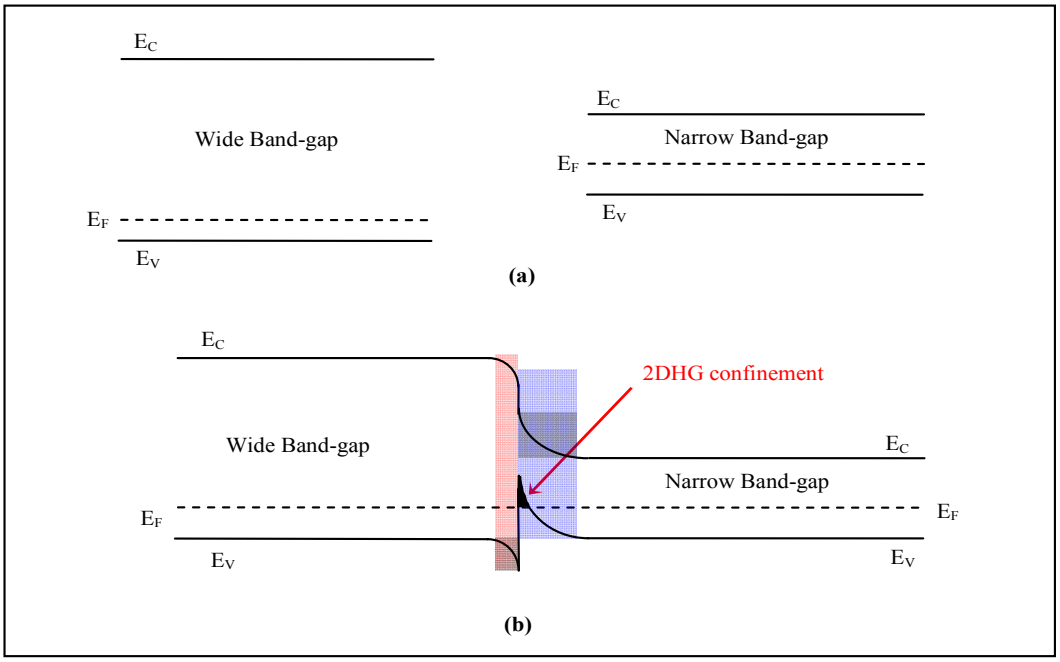

Figure 2-2: P-type wide band-gap and a low-doped narrow band-gap semiconductor (a) isolated and (b) in contact

For heterojunctions with two-dimensional sheet charge confinement, the current path normal to the semiconductor-semiconductor interface in the host material will be a function of the material's charge mobility. Characteristic of a sheet charge that is produced within an intrinsic or low-impurity semiconductor, impurity scattering effects are minimized thus charge mobility is relatively larger in these regions than in highly doped regions [27].

Current transport along the degenerate heterojunction interface will be a function of the host material's sheet charge concentration within the potential well as well as its charge mobility. Charge confinement is effectively normal to the semiconductor-semiconductor interface and exists within the narrow band semiconductor. Heavily

doping the wide band-gap material will increase charge confinement and create a deeper, highly concentrated, potential well.

2.2. Degenerate Metal-Semiconductor Contacts

Metal-semiconductor (MS) contacts come in two forms; ohmic and rectifying. Ohmic MS contacts allow charge carriers to cross the interface nearly un-rectified. This is due to the electron concentration above the semiconductor's conduction band which is comparable to that of a metal. Rectifying MS devices, otherwise known as Schottky diodes, macroscopically act as typical PN diodes but with an order of magnitude increase in dark current.

For metal-semiconductor contacts with 2DEG confinement, a current parallel to the metal-semiconductor interface will be a function of the electron mobility and doping concentrations within the host semiconductor. Note that the current path for an in-plane Schottky contact device, which will be discussed later, is normal to the metal-semiconductor interface and can be schematically and electrically modeled as two Schottky diodes in a front-to-front configuration. Thus the reverse-bias Schottky diode current becomes the limiting current factor which determines the overall current flow through the two-dimensional system.

Thermionic emission current and thermionic field emission current are the two types of current flow through a metal-semiconductor interface with the latter being more dominant in degenerate devices. Describing the current normal to the metal-semiconductor interface, the net current density can be written in the following form:

$$J(V_a) = J_f(V) - J_r(V) = A^{**}T^2 e^{\left(\frac{-q\phi_{bi}}{k_B T}\right)}\left(e^{\left(\frac{qV_{bias}}{k_B T}\right)} - 1\right) \quad (1)$$

In the above equation, J_f and J_r are the forward and reverse bias current densities, respectively, T is the temperature, ϕ_{bi} is the built-in potential at the metal-semiconductor interface, and A^{**} is the Richardson constant and is defined as:

$$A^{**} = \alpha\left(\frac{m_n q k_b^2}{2\pi^2\hbar^2}\right) \quad (2)$$

For the Richardson constant, m_n is the effective mass and α is an empirical factor on the order of unity; for gallium arsenide (GaAs), A^{**} = 4.4 A/(cm^{2}K^2).

With all the discussed metal-semiconductor-metal devices in this thesis study schematically represented as two Schottky contact junctions in front-to-front form, focus is on the reverse biased Schottky contact as this is the current-limiting junction which determines the overall current flow of the device.

2.2.1. Thermionic Emission

Illustrated in Figure 2-3, electrons travel over the built-in potential barrier closer to the barrier's peak; this is otherwise known as thermionic emission. For a rectifying contact with low to moderate doping thermionic emission current is more dominant [27].

Thermionic emission theory assumes that electrons that have energies larger than the top of the potential barrier will cross provided they drift towards the barrier [26].

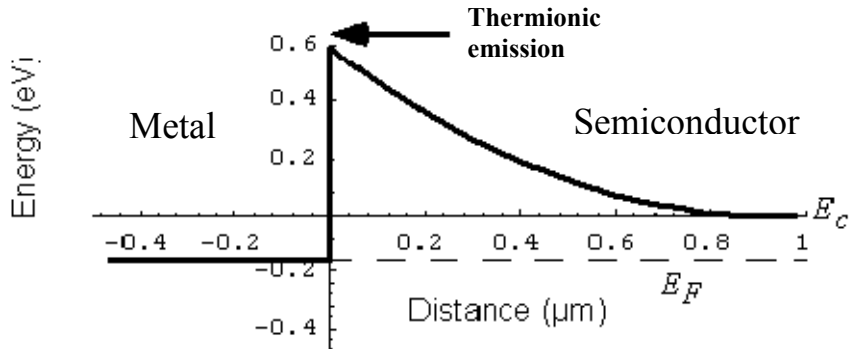

Figure 2-3: Energy band diagram of Schottky barrier junction for GaAs with doping level $N_D = 10^{15}/cm^3$; from [32]

Since the Schottky barrier height is relatively smaller than the barrier height in *p-n* junction diodes under similar conditions the diode saturation current, defined as I_s, is typically larger for Schottky diodes with Schottky barrier heights approximately two-thirds of the host material's energy gap or less. The specific contact resistance (R_c) for thermionic emission current is given by:

$$R_c = \frac{\left(\frac{kT}{q}\right) \cdot \exp\left(\frac{q\phi_{bi}}{kT}\right)}{A^* T^2} \tag{3}$$

Thus, the specific contact resistance decreases rapidly as the barrier height decreases. As the doping concentration increases, the probability of thermionic emission and field emission decrease and increase, respectively [27].

2.2.2. Thermionic Field Emission (Tunneling)

Figure 2-4 shows the depletion region in a highly doped N-type semiconductor. This region is so narrow, electrons can tunnel through the barrier at energies lower than the barrier height of the device; a process otherwise known as thermionic-field emission [27]. The space charge width in a rectifying MS contact is inversely proportional to the square root of the semiconductor doping; as doping concentration increases, the probability of tunneling increases. The number of electrons with energies above a given energy E_o decreases in energy proportional to $\exp[-E/(k_B T)]$ Most notably, the barrier transparency increases exponentially with the decrease in the barrier width. The barrier becomes thinner and the dominant electron tunneling path occurs at lower energies than the top of the barrier for high impurity concentrations [32].

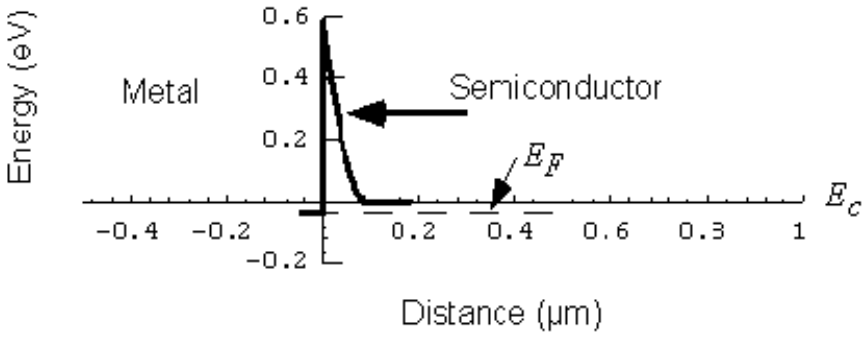

Figure 2-4: Energy band diagram of Schottky barrier junction for GaAs with doping level $N_D = 10^{17}/cm^3$; from [32]

In degenerate semiconductors with a small electron effective mass such as the GaAs, electrons can tunnel through the barrier either at or near the device Fermi level, and the tunneling current is most dominant (see Figure 2-5).

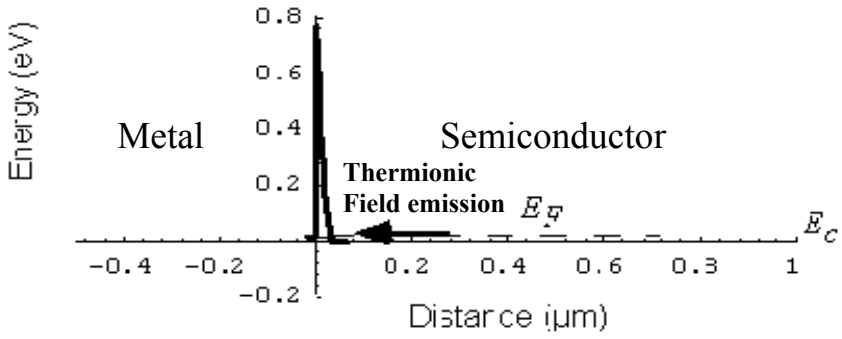

Figure 2-5: Energy band diagram of Schottky barrier junction for GaAs with doping level $N_D = 10^{18}/cm^3$; from [32]

Similar to the thermionic model of a Schottky diode, the current-voltage characteristic of thermionic-field emission can be calculated using the same approach but with the exception that the product of the tunneling transmission coefficient and the

number of electrons at a given energy as a function of energy integrate over the states in the conduction band must be evaluated [32]. The current density in the thermionic-field emission regime under forward bias is defined as:

$$j = j_{stf} \exp\left(\frac{qV_{bias}}{E_o}\right), \tag{4}$$

where E_o and j_{stf} are defined as the following:

$$E_o = E_{oo} \coth\left(\frac{E_{oo}}{k_b T}\right) \tag{5}$$

$$E_{oo} = \frac{qh}{4\pi}\sqrt{\frac{N_d}{m_n \varepsilon_s}} \tag{6}$$

$$j_{stf} = \frac{A^* T \sqrt{\pi\left(\phi_{bi} - qV_{bias} - E_c + E_{F,n}\right)}}{k_b \cosh\left(E_{oo}/k_b T\right)} \exp\left[-\frac{E_c - E_{F,n}}{k_b T} - \frac{\left(\phi_{bi} - E_c + E_{F,n}\right)}{E_o}\right] \tag{7}$$

Note that for a GaAs Schottky diode, the thermionic-field emission becomes important for donor-doping concentration $N_D > 10^{17}/\text{cm}^3$ at 300 K and for $N_D > 10^{16}/\text{cm}^3$ at 77 K. For silicon, the corresponding values of N_D are several times larger. Figure 2-6 gives the forward J-V characteristics of GaAs Schottky diodes at various doping levels [32].

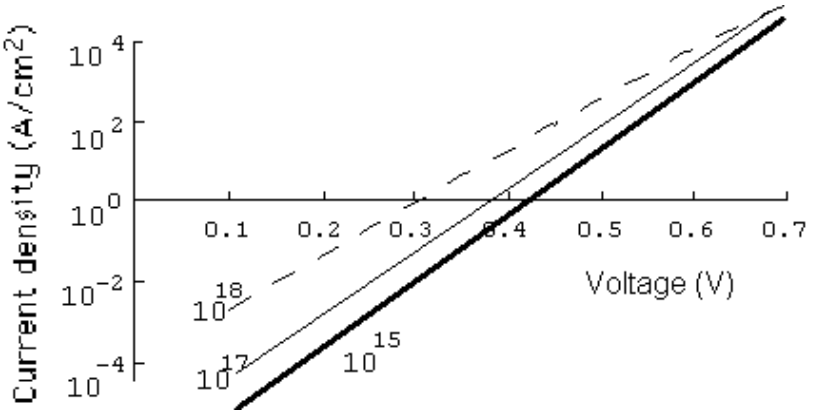

Figure 2-6: Forward J-V characteristics of GaAs Schottky diodes doped at 10^{15}/cm^3, 10^{17}/cm^3, and 10^{18}/cm^3 at T = 300 K; from [32]

The resistance of the Schottky barrier; in the field emission regime is relatively low. Therefore metal-semiconductor contacts (n^+) are used as ohmic contacts. The specific contact resistance decreases with an increase in doping of the semiconductor.

Including the electron-beam induced current (EBIC) method, the theory of electron detection in delta modulation-doped metal-semiconductor-metal heterostructure devices under electron beam perturbation is discussed. In support of this device type study, data analysis of 2DHG EBIC device characterization is also given. In-plane Schottky contact/2DEG devices are also theoretically discussed but devices of this type were not readily available.

2.3. Device Physics

There has been numerous theoretical evaluations conducted focusing on the transport properties for mesa-etched Schottky contact devices. However, for this thesis

study, a major focus is placed on the transport properties of charge carriers within a heterojunction metal-semiconductor-metal structure.

2.3.1. In-Plane Schottky Contact Device

With the current flow of an in-plane Schottky contact/2DEG device passing from metal to semiconductor along the electron gas sheet plane, the device is considered a two-dimensional system. Schematically this device is represented by placing two Schottky diodes in a front-to-front configuration (see Figure 2-7).

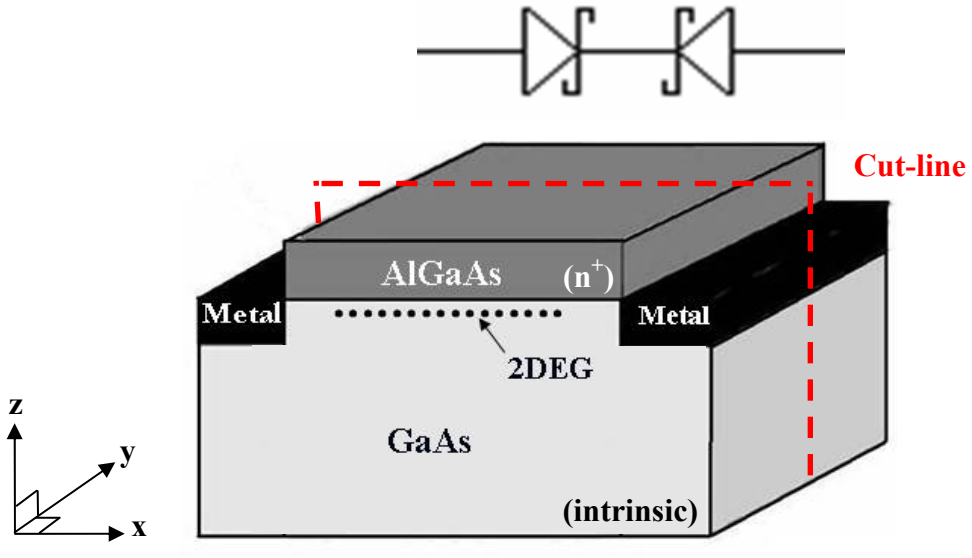

Figure 2-7: Illustration of In-plane Schottky contact/2DEG device in equilibrium [7]

There are three conditions for in-plane Schottky contact/2DEG devices that are of importance for electron detection using the EBIC method; devices in thermal equilibrium, devices under bias, and electron-perturbed devices under bias. Note that all band-

bending diagrams are representative of the device along the x-z plane cut-line illustrated in Figure 2-7.

2.3.1.1. Device in Thermal Equilibrium

Figure 2-8 and Figure 2-9 illustrate unbiased in-plane Schottky contact, non-degenerate and degenerate devices, respectively, in thermal equilibrium along the cut-line. For such devices, the net current is zero, and both have symmetrical depletion-region, Schottky contact pairs. The depletion regions are calculated as functions of the doping concentration of the GaAs substrate. With degenerate devices, a 2DEG sheet charge exists at the AlGaAs/GaAs interface typically with an intrinsic GaAs host.

Typical for unbiased Schottky/n-type semiconductor contact interfaces, the depletion widths W_L and W_H can be calculated using

$$W = \left[\frac{2\varepsilon_s V_{bi}}{qN_D} \right]^{1/2}, \tag{8}$$

where ε_s is the relative permittivity of the semiconductor, V_{bi} (also referred to as V_{B0} for undoped semiconductors) is the built-in potential, and N_D is the donor impurity concentration for the interfacing semiconductor. Calculating the ideal Schottky barrier height (φ_{B0}), the metal's work function (φ_m) and electron affinity (χ) of the semiconductor is needed. Thus for a gold contact/ moderately-doped gallium arsenide (Au/GaAs)

interface with $N_D = 3 \times 10^{15}$ cm^{-3}, $V_{bi} = 0.899$ V, $\varepsilon_s = 1.1 \times 10^{-12}$ F/cm, the depletion width is calculated to be:

$$W_L = \left[\frac{2\varepsilon_s V_{bi}}{qN_D}\right]^{1/2} = \left[\frac{2 \cdot 12.9 \cdot (8.85x10^{-14}) \cdot 0.899}{(1.6x10^{-19}) \cdot (3x10^{15})}\right]^{1/2} = 6.54x10^{-5} cm = 0.654 \mu m$$

For a gold contact/ degenerate gallium arsenide interface with $N_D = 3 \times 10^{18}$ cm^{-3}, $V_{bi} = 1.08$ V the depletion width is calculated to be:

$$W_H = \left[\frac{2\varepsilon_s V_{bi}}{qN_D}\right]^{1/2} = \left[\frac{2 \cdot 12.9 \cdot (8.85x10^{-14}) \cdot 1.08}{(1.6x10^{-19}) \cdot (3x10^{18})}\right]^{1/2} = 2.27x10^{-6} cm = 0.0227 \mu m$$

As stated in section 2.2.2, the probability of thermionic field emission, or tunneling, is proportional to semiconductor doping concentration; typical for degenerate contacts [27].

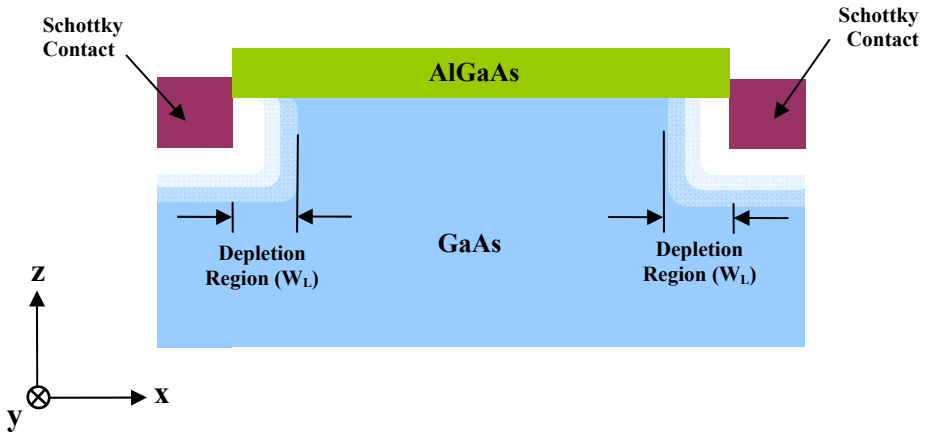

Figure 2-8: Non-degenerate in-plane Schottky contact device in thermal equilibrium along cut-line (not-to-scale)

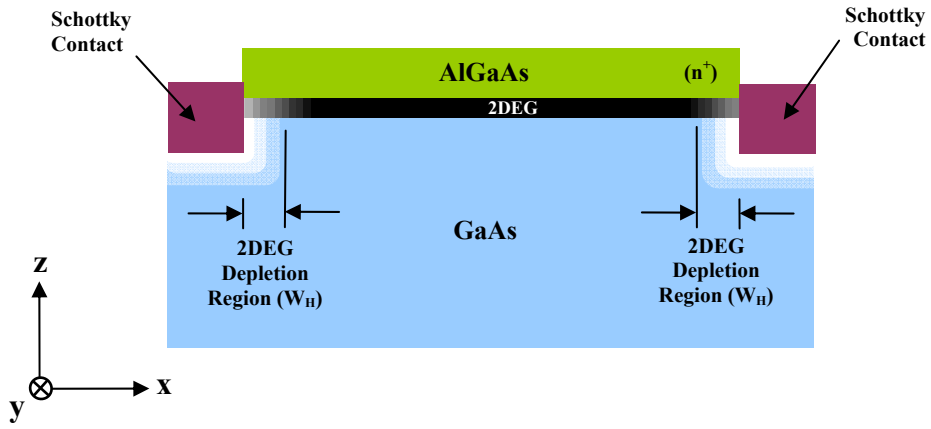

Figure 2-9: Degenerate in-plane Schottky contact/2DEG device in equilibrium along cut-line (not-to-scale)

Figure 2-10 and Figure 2-11 are band-bending illustrations of the in-plane Schottky contact, non-degenerate and degenerate devices, respectively, in equilibrium. The depletion widths W_L, assumed ideally symmetrical with identical metal contacts, are formed when the metal comes in contact with the non-degenerate host semiconductor. Although the illustrations are not to scale, note that the depletion width, or barrier thickness, for the degenerate device (W_H) is relatively thinner than the non-degenerate device (W_L) with the two-dimensional sheet charge confined between the depletion regions formed at the metal-semiconductor interfaces (see Figure 2-11). Hasegawa, *et al.,* discuss quantum device fabrication with similar in-plane gate (IPG) 2DEG configuration confining methods [18].

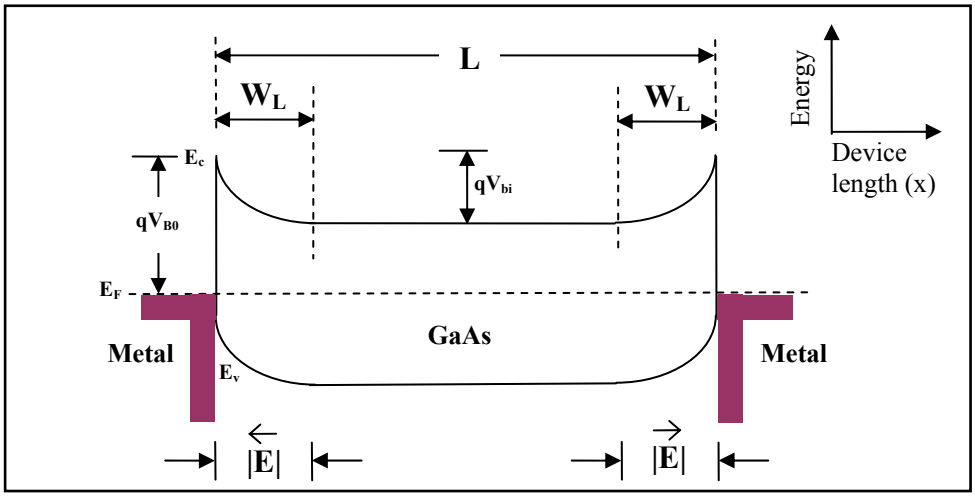

Figure 2-10: Non-degenerate in-plane Schottky contact energy band diagram along cut-line in equilibrium

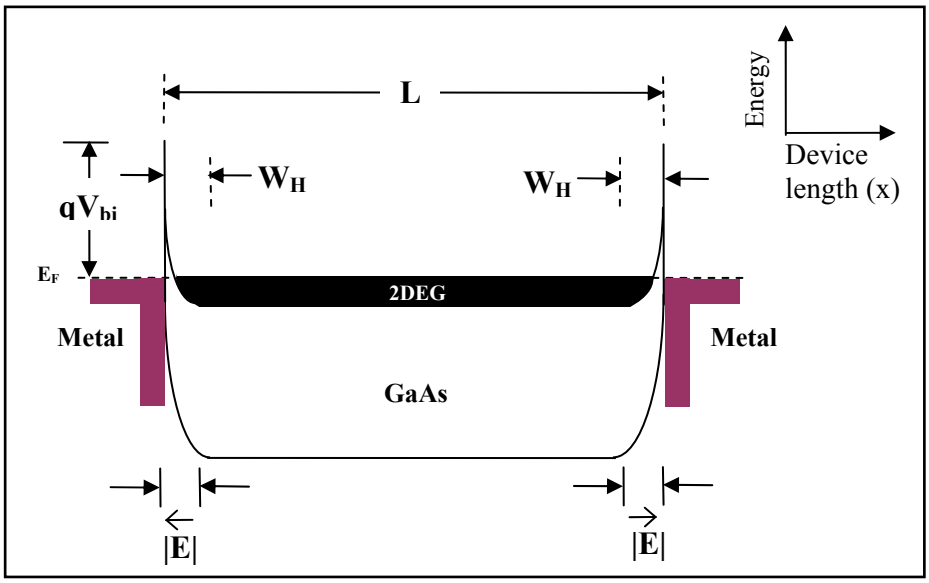

Figure 2-11: Degenerate in-plane Schottky contact/2DEG energy band diagram along cut-line in equilibrium

2.3.1.2. Device Under Bias

Non-degenerate and degenerate in-plane Schottky contact devices under bias are illustrated in Figure 2-12 and Figure 2-13, respectively. Typically for n-type semiconductors, electrons meet a potential barrier wall qV_{bi} when passing from the semiconductor to the metal contact in a non-degenerate device at the forward biased junction (see Figure 2-5). For such devices, the net current is dominated by thermionic emission; electrons with enough energy to mount the barrier height can enter the metal contact. From previous studies, it has been proven that an electric field exists throughout the entire length L of the host semiconductor that lies between the electrodes in non-degenerate devices when the flat-band condition is met.

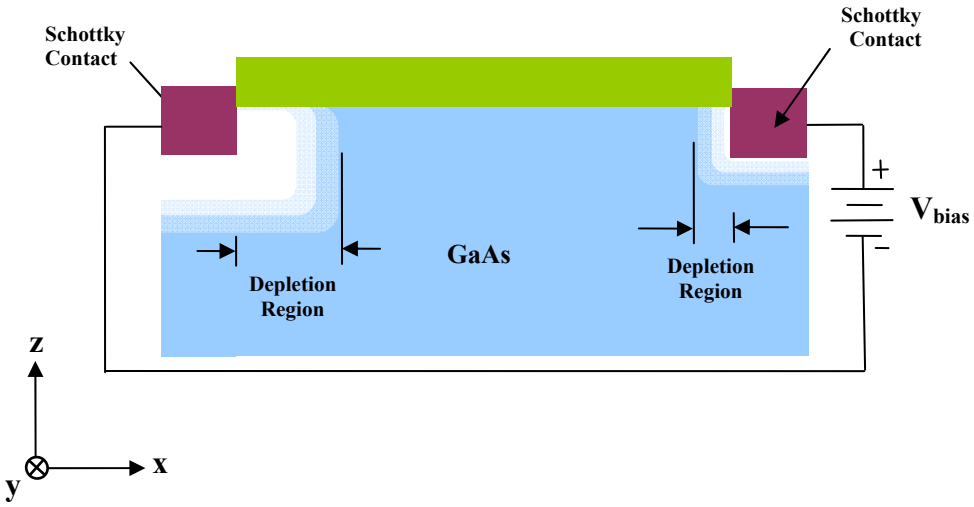

Figure 2-12: Non-degenerate in-plane Schottky contact device along cut-line under bias (not-to-scale)

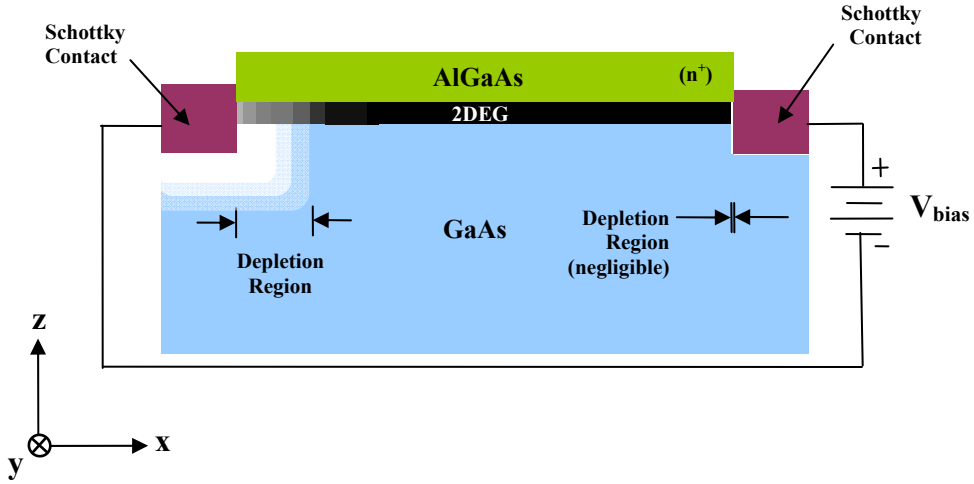

Figure 2-13: Degenerate in-plane Schottky contact/2DEG device along cut-line under bias (not-to-scale)

With its high sheet carrier concentration, the two-dimensional electron gas in degenerate devices act as an equi-potential plane that forces the external potential to drop across the depletion region at the reverse bias junction. The net current is dominated by thermionic field emission or quantum mechanical tunneling; electrons tunnel through the relatively thin potential barrier at energies lower than the barrier height at the forward biased junction. An interesting property of the Schottky/2DEG contact is the metal-semiconductor interface is ohmic; charge carriers can pass from metal-to-semiconductor and vice versa virtually un-rectified. Thus the 2DEG acts as an anode that extends deeper into the device [22].

Typical for biased metal-semiconductor (n-type) contact interfaces, Neaman [27] states the reverse-biased junction depletion width can be calculated using

$$W = \left[\frac{2\varepsilon_s (V_{bi} + V_a)}{qN_D}\right]^{1/2}, \tag{9}$$

where $V_a = |V_{bias}|$, the magnitude of the applied bias; biasing-dependant depletion width modulation is most effective at the reverse-biased junction. The forward biased junction depletion region is only marginally affected at biasing levels below the reach-through biasing potential V_{RT}. Thus for a gold contact, moderately-doped gallium arsenide (Au/GaAs) interface with $N_D = 3 \times 10^{15}$ cm^{-3} and $V_{bias} = 1$V, $V_{bi} = 0.899$ V, $\varepsilon_s = 1.11 \times 10^{-12}$ F/cm, the reverse-biased depletion width, $W_{L,RevB}$, is calculated:

$$W_{L,RevB} = \left[\frac{2\varepsilon_s (V_{bi} + V_a)}{qN_D}\right]^{1/2} = \left[\frac{2 \cdot 12.9 \cdot (8.85x10^{-14}) \cdot (1 + 0.899)}{(1.6x10^{-19}) \cdot (3x10^{15})}\right]^{1/2} = 9.50x10^{-5} cm = 0.950 \mu m$$

For a gold contact, degenerate gallium arsenide interface with $V_{bias} = 1$V and $N_D = 3 \times 10^{18}$ cm^{-3}, the reverse biased depletion width, $W_{H,RevB}$, is calculated:

$$W_{H,RevB} = \left[\frac{2\varepsilon_s (V_{bi} + V_a)}{qN_D}\right]^{1/2} = \left[\frac{2 \cdot 12.9 \cdot (8.85x10^{-14}) \cdot (1 + 1.08)}{(1.6x10^{-19}) \cdot (3x10^{18})}\right]^{1/2} = 3.14x10^{-6} cm = 0.0314 \mu m$$

Note that the probability of thermionic field emission in the degenerate device at the forward-biased interface is proportional to biasing due to the narrowing of the depletion region; the depletion region becomes negligibly small with higher biasing [27].

Figure 2-14 is an example of undoped-device energy band-bending under bias in its reach-through stage; potential reach-through biasing ($\boldsymbol{V_{RT}}$) causes the depletion regions to overlap. As potential biasing increases, the device approaches its flat-band stage and the depletion width $\boldsymbol{x_m}$ approaches zero. Figure 2-15 is an example of a device under bias in its flat-band stage; potential flat-band biasing ($\boldsymbol{V_{FB}}$) has formed a single depletion region within the host semiconductor and a constant electric field exists throughout the device length. Electrons pass from the semiconductor to the forward biased contact and holes pass from the semiconductor to the reverse biased contact unhampered.

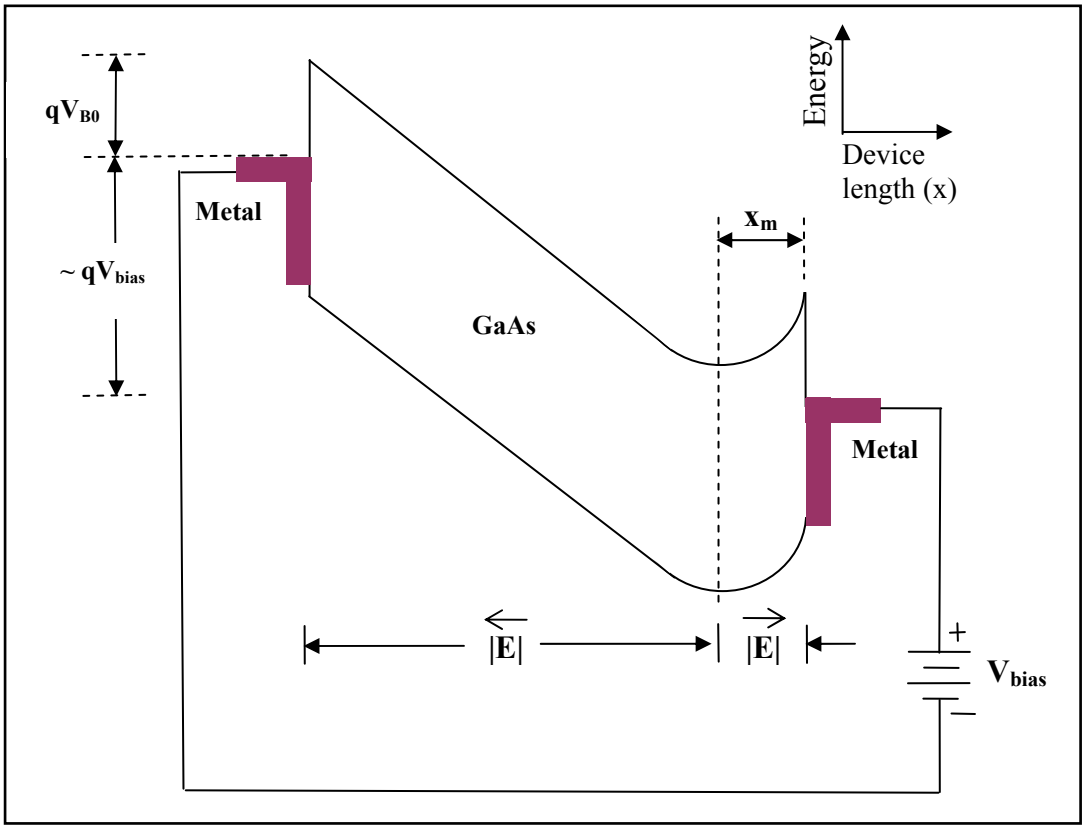

Figure 2-14: Non-degenerate in-plane Schottky contact energy band diagram along cut-line under bias ($|V_{RT}| < |V_{bias}| < |V_{FB}|$, $x_m <$ unbiased W_L)

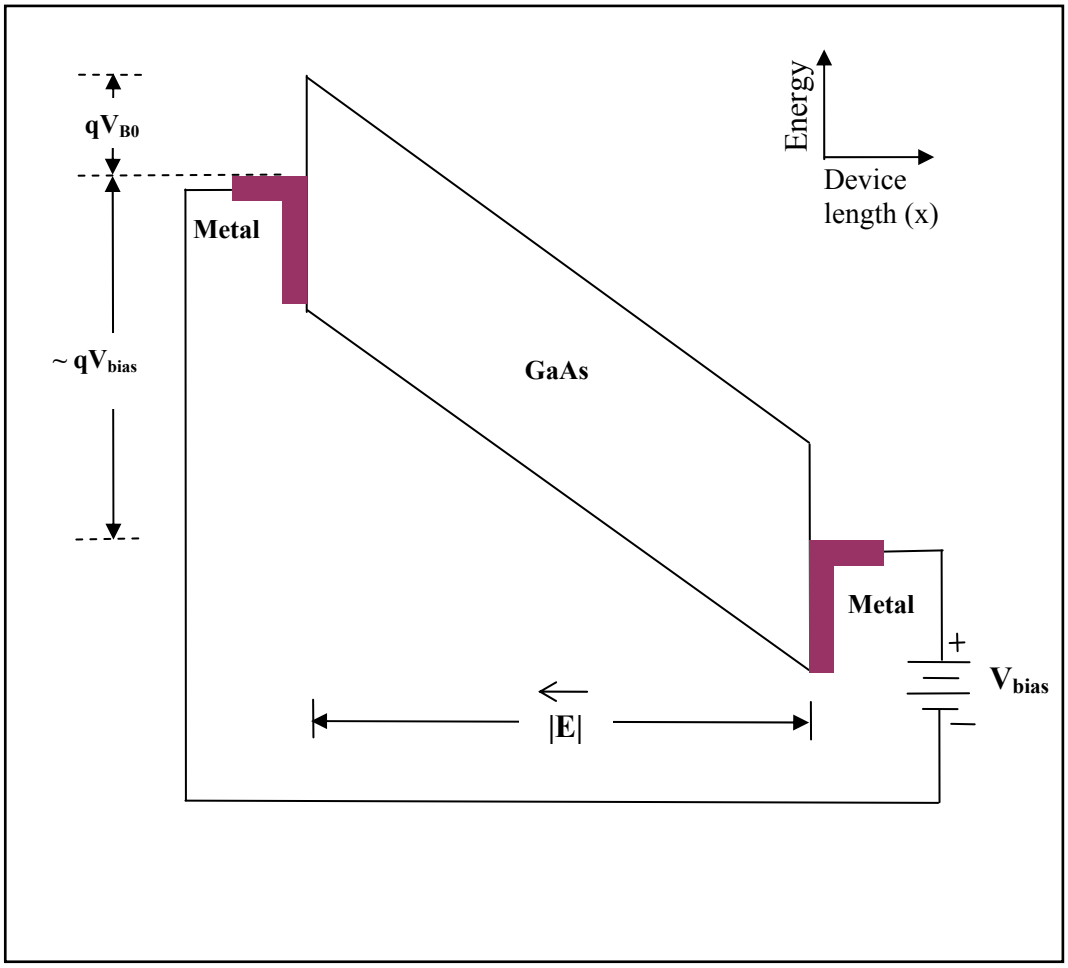

Figure 2-15: Non-degenerate in-plane Schottky contact device energy band diagram under bias ($|V_{bias}| > |V_{FB}|$)

Relative to a biased, non-degenerate device with identical device dimensions, the biasing potential is dropped across a smaller depletion region in the degenerate device which produces a stronger electric field. Experimental results measuring sheet charge potential proved that an electric field does not exist in the electron gas; the 2DEG sheet is held at the same potential as the forward biased junction which acts as an extension to this electrode (see Figure 2-16) [22].

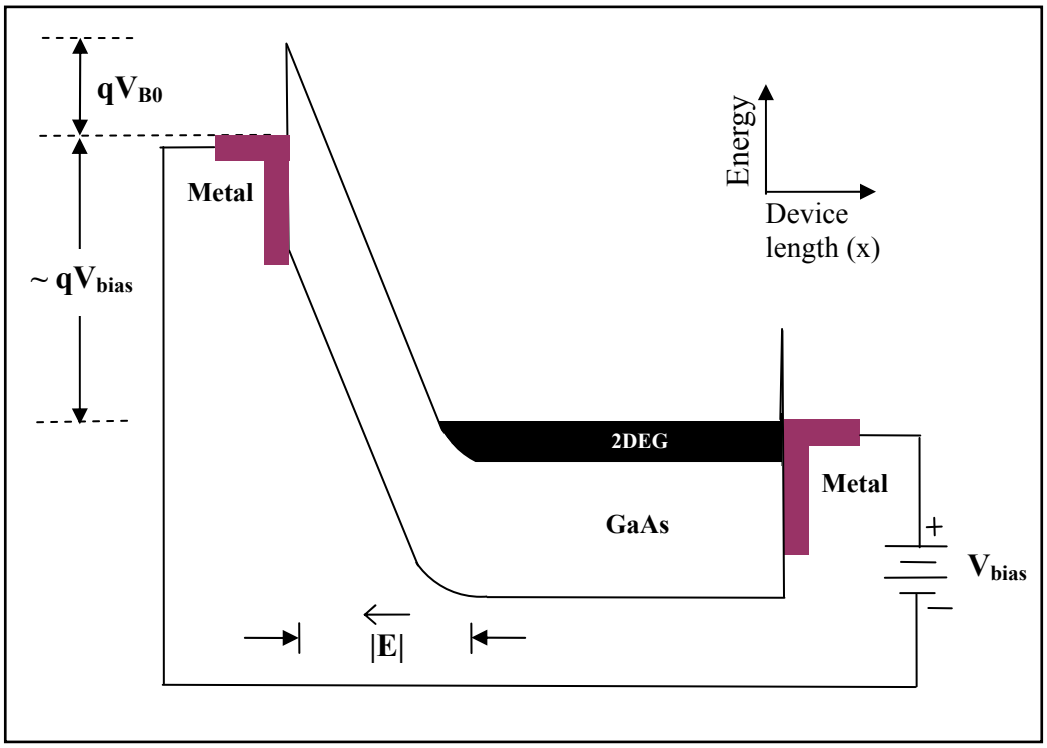

Figure 2-16: Degenerate in-plane Schottky contact/2DEG energy band diagram under bias

2.3.2. HMSM Device

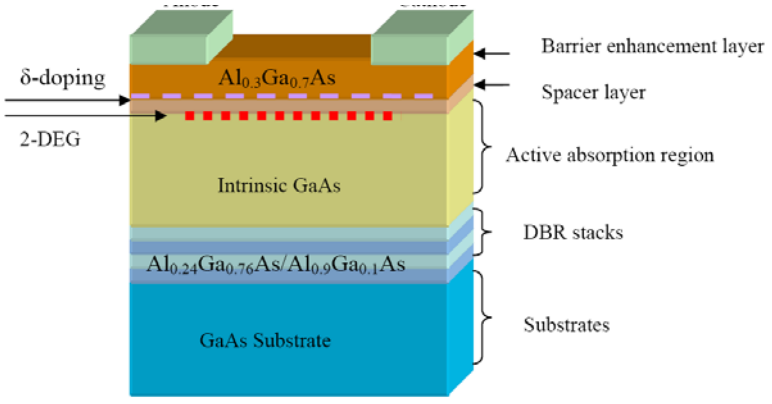

Figure 2-17: Detailed cross section of 2DEG-based resonant-cavity-enhanced (RCE) MSM photo-detector; from [45]

An AlGaAs/GaAs based resonant-cavity-enhanced (RCE) Heterostructure MSM (HMSM) photodetector with $Al_{0.24}Ga_{0.76}As/Al_{0.9}Ga_{0.1}As$ Distributed-Bragg-Reflector (DBR) fabricated at Consiglio Nazionate delle Recerche (CNR)/Istituto per la Microelectronica ed I Microsistemi (IMM) in Italy, and grown by IQE, Inc., was characterized for this study. Figure 2-20 illustrates the top-view of the HMSM structure electrodes which consists of an anode and cathode in a repetitively inter-digitated configuration when biased. This vertical transit-time limited monolithic resonant-cavity-enhanced (RCE) MSM photodetector is constructed for 850-nm wavelength detection [45].

Metal Schottky contacts are deposited to form the inter-digitated anode and cathode fingers. Illustrated in Figure 2-20, the length of the aforementioned finger *L* is 40 μm with a 2 μm finger width *W*, and a 2 μm finger separation *G*. The active region is approximately 40x40 μm^2 (1 μm thick for unit cell) [7]. The field-dependent intrinsic electron drift velocities for the GaAs absorption region of the device described above at 300K are given in Figure 2-18 [45].

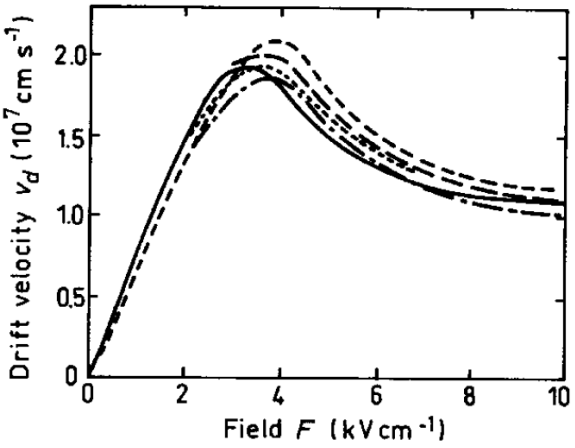

Figure 2-18: Electron drift velocities vs. E-field at 300K for GaAs; from [45]

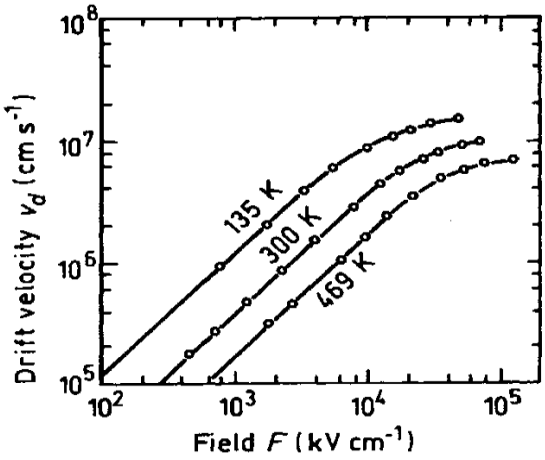

Figure 2-19: Hole drift velocity vs. E-field at varying temperatures for GaAs; from [45]

With this repetitive pattern, a simplified unbiased version of each neighboring anode/cathode cell is given in Figure 2-21. All band-bending diagrams are representative of the device along the y-z plane cut line. As a reference, the anode/cathode nomenclature is defined with the anode being the electrode supplying positive current (holes) while the cathode supplies negative current (electrons) and is based on the biasing hardware and not the test device.

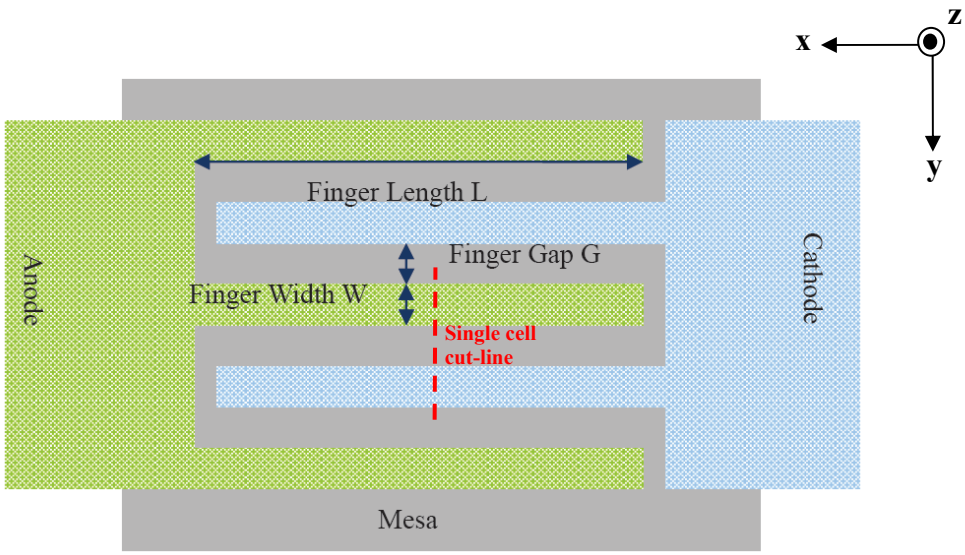

Figure 2-20: Top-view of inter-digitated HMSM device [45]

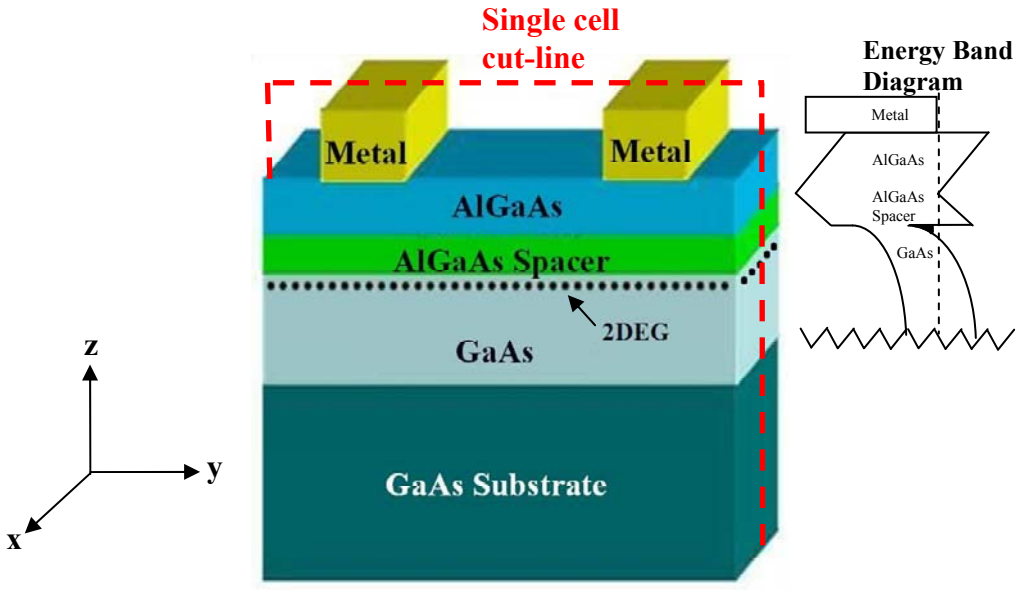

Figure 2-21: Simplified 3-D illustration of delta modulation doped HMSM device and its energy band diagram along its cut-line in equilibrium [45]

There are three conditions for the HMSM devices that are of importance for electron detection using the EBIC method; devices in thermal equilibrium, devices under bias and devices under bias and electron beam perturbation. EBIC data collection for these devices can be used to determine the effects of using delta modulation doped HMSM devices relative to the undoped equivalent. Note that all band-bending diagrams are representative of the device along the y-z plane cut-line illustrated in Figure 2-21; Figure 2-22 illustrates the device dimensions at the indicated single-cell cut line.

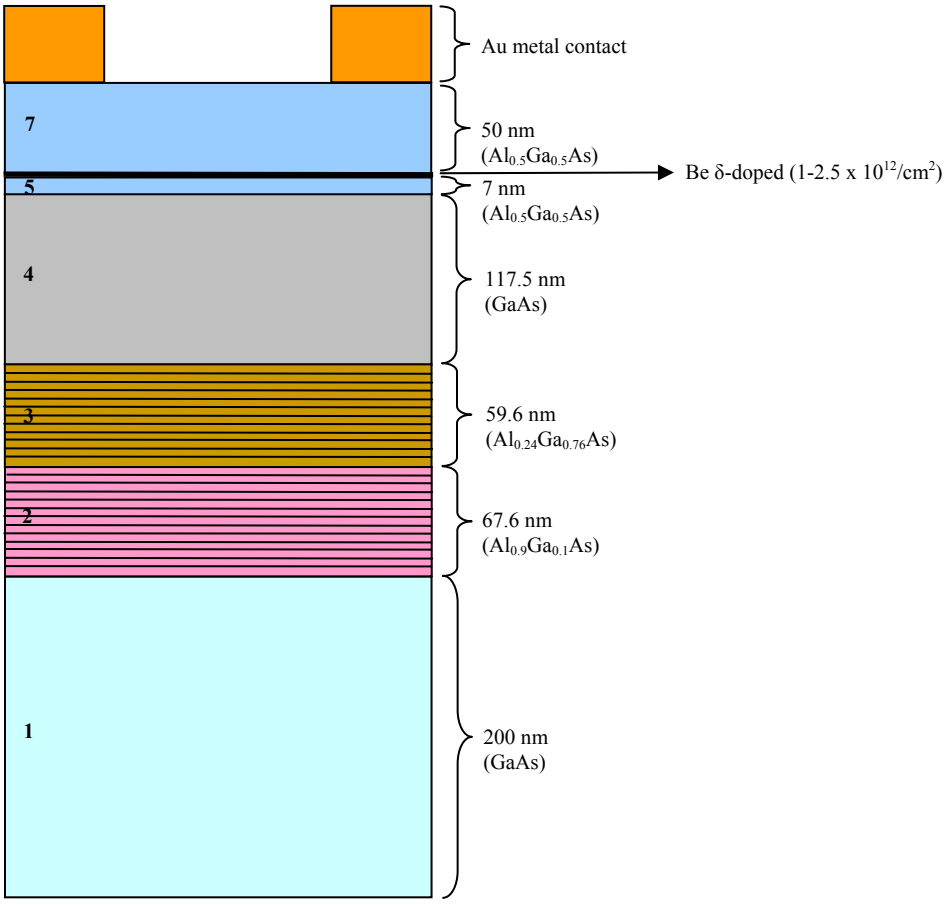

Figure 2-22: Layer dimensions of delta modulation doped HMSM device [45]

Table 2-1: Layered structure for 2-DHG device in Figure 2-22 [45]

Layer #	Thickness	Material	Specification
7	50 nm	$Al_{0.5}Ga_{0.5}As$	barrier enhancement layer
6	Be δ-doped		1-2.5 x $10^{12}/cm^2$
5	7 nm	$Al_{0.5}Ga_{0.5}As$	undoped spacer
4	117.5 nm	GaAs	absorption layer
3	59.6 nm	$Al_{0.24}Ga_{0.76}As$	15 wells for Bragg Reflection
2	67.6 nm	$Al_{0.9}Ga_{0.1}As$	15 wells for Bragg Reflection
1	200 nm	GaAs	buffer
0	2"	GaAs	semi-insulating substrate (not shown)

Table 2-2: Calculated Semiconductor Parameters [27] [1]

	Semiconductor Parameters				
	μ_n (cm^2/Vs)	μ_p (cm^2/Vs)	? (eV)	e_r or (1+? $_e$)	V_{B0} (Au contact)
GaAs	8500	400	4.07	12.9	1.03 V
$Al_{0.5}Ga_{0.5}As$	145	70	3.57	11.5	1.53 V
$Al_{0.24}Ga_{0.76}As$	330	180	3.81	12.2	1.29 V
$Al_{0.9}Ga_{0.1}As$	206	96	3.51	10.3	1.59 V

Although generated charge carriers can exist in different layers of the device under electron-beam perturbation, Table II-2 indicates the carriers experience a much higher mobility in the GaAs layer, thus carriers in this layer can have a higher contribution to total current within the device.

2.3.2.1. Device in Thermal Equilibrium

Each delta modulation-doped HMSM device in thermal equilibrium has a similar energy band diagram depicted in Figure 2-33. Delta-doping within the device produces a confined electron cloud and an associated transverse electric field.

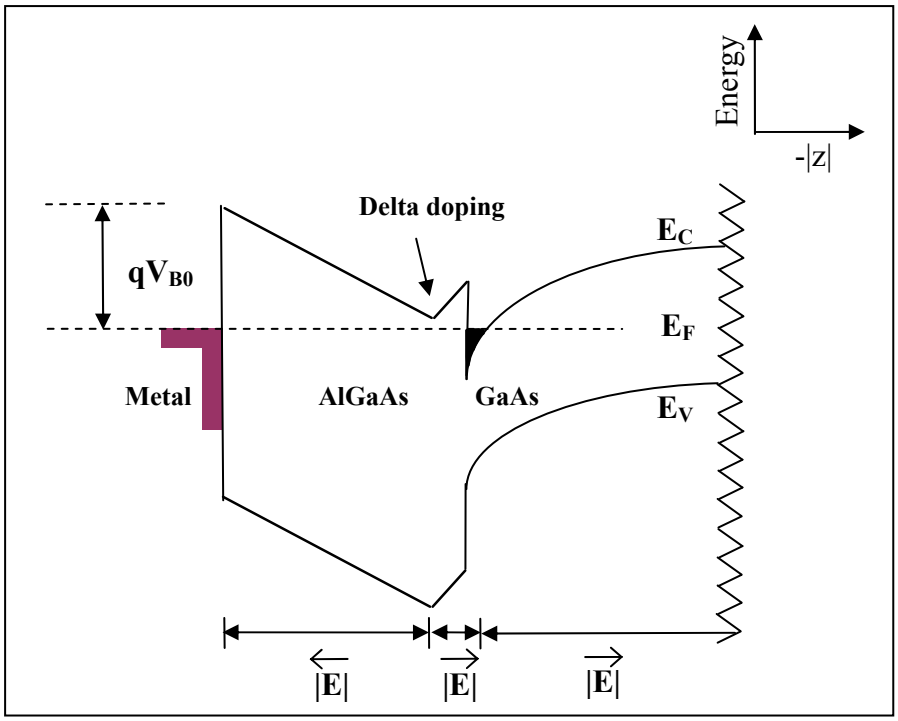

Figure 2-23: HMSM energy band diagram in equilibrium under electrode

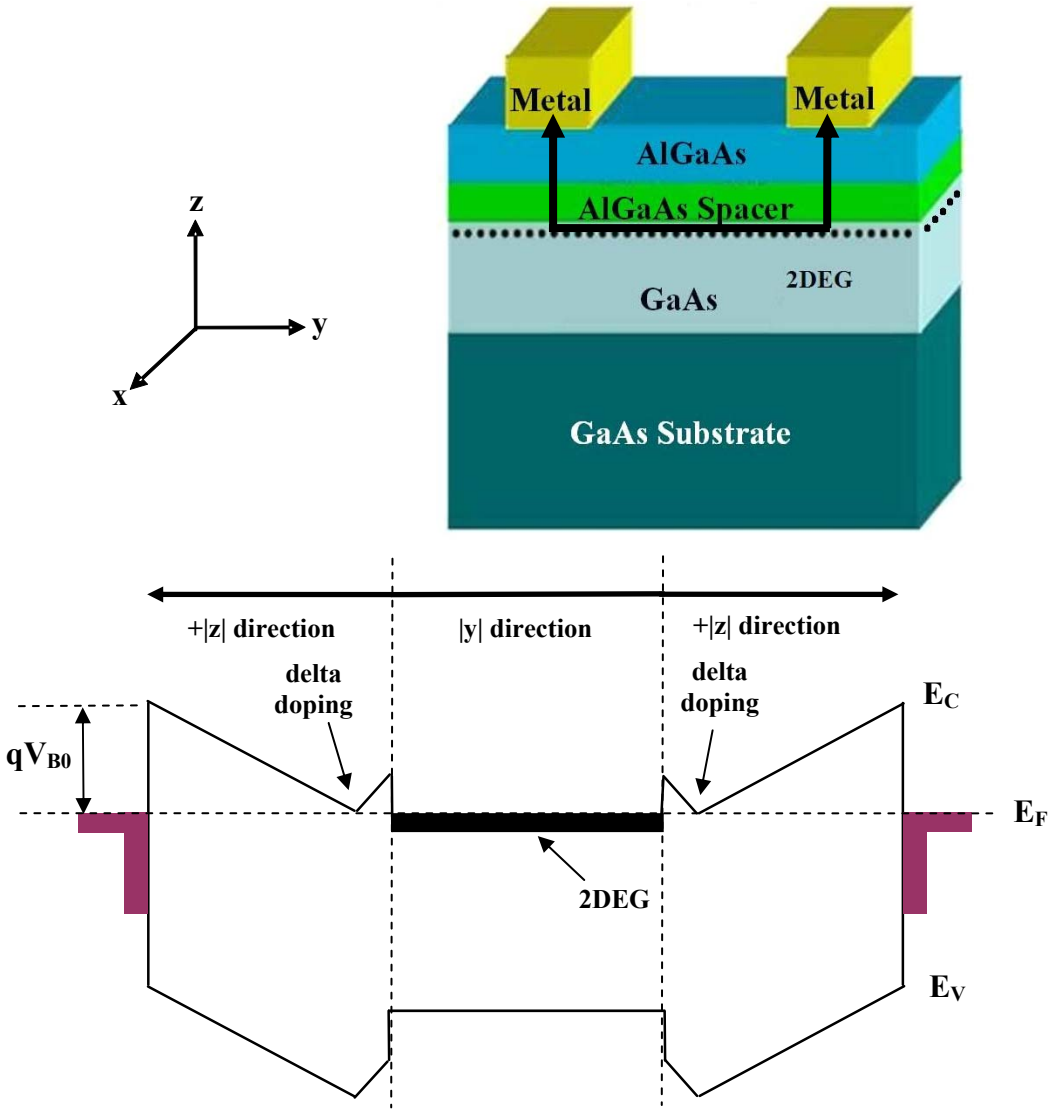

Figure 2-24: Equilibrium energy band diagram of 2-D HMSM current path mapped to 1-D with z-direction exaggerated for clarity (not-to-scale) [45]

2.3.2.2. Device Under Bias

Upon biasing and preceding the critical point of flat-band, a large portion of the applied bias is expected to drop at the reverse-biased junction of the device and a negligible potential bias exists at the forward biased junction. Charge energy

redistribution is the dominant electron transport factor for optically generated electrons within the two-dimensional gas; energy transport along the 2-DEG is much faster process than electron transport by drift. Thus the 2DEG sheet charge effectively serves as an extended contact for the collection of carriers [45].

High electron concentration at the AlGaAs/GaAs interface prevents the depletion region to extend into the two-dimensional sheet charge. The two-dimensional depletion width is calculated with

$$d_{2d} = \frac{2\varepsilon_s (V_{bi} + V_a)}{qn_s}, \tag{10}$$

where $V_a = |V_{bias}|$ is the applied bias, V_{bi} is the built-in potential of the Schottky contact junction, and n_s is the sheet carrier density for a two-dimensional system. Thus a delta-doped device ($5\text{x}10^{12}/\text{cm}^2$ doping level) producing a 2DEG concentration of $n_s \approx 2.5\text{x}10^{12}/\text{cm}^2$ [45] and biased to $V_{bias} = 1$ V, then $V_{bi} = 1.53$ V and $d_{2d} = 0.129$ μm. For the three-dimensional depletion width, d_{3d} is calculated with

$$d_{3d} = \sqrt{\frac{2\varepsilon (V_{bi} + V_a)}{qn_v}}, \tag{11}$$

where n_v is the sheet carrier volume for a three-dimensional system (approximated to be $10^{15}/\text{cm}^3$). Thus a delta-doped device ($5\text{x}10^{12}/\text{cm}^2$ doping level) producing a 2DEG concentration of $n_v \approx 10^{15}/\text{cm}^3$ and biased to $V_{bias} = 1$ V, then $V_{bi} = 1.53$ V and $d_{3d} = 1.79$ μm. Note that the photocurrent in the device reaches saturation at external biasing greater than 1.5 V [45].

Table 2-3: Calculated depletion widths for delta doped HMSM

V_{bias} (V)	d_{2d} (μm)	d_{3d} (μm)
0	0.078	1.40
1	0.129	1.79
2	0.180	2.12
3	0.231	2.40
4	0.281	2.65
5	0.332	2.88

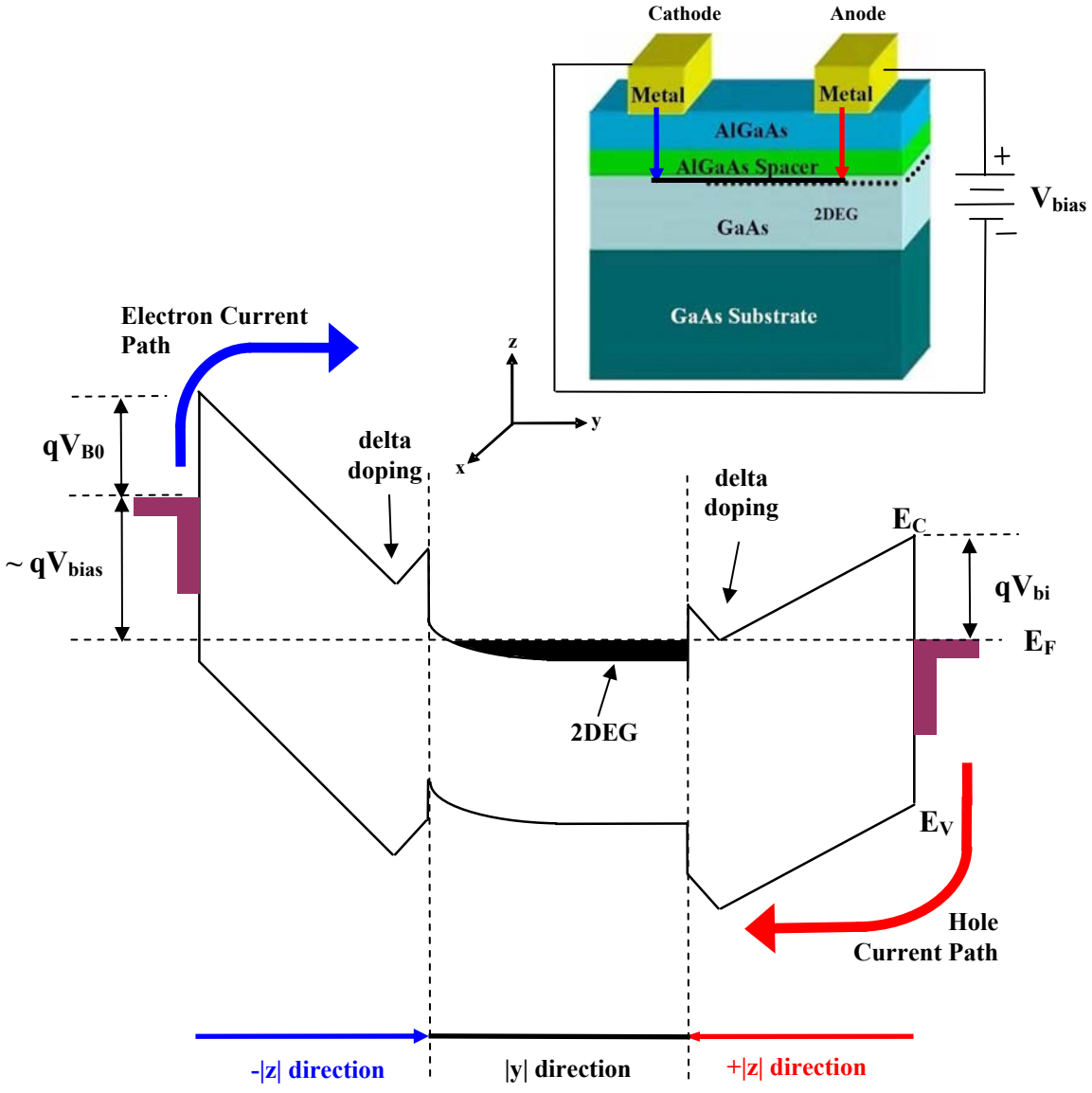

Figure 2-25: Biased energy band diagram of 2-D HMSM current path mapped to 1-D with z-direction exaggerated for clarity (not-to-scale) [45]

2.3.2.3. Metal-Semiconductor-Metal Applications

The Army Research Labs (ARL) derived a frequency modulated continuous wave (FMCW) profiler using an MSM setup (see Figure 2-23). This application is useful for surveillance application from a low flying unmanned aerial vehicle. It has the ability to depict multiple targets within a pixel and is ideal for cluttered situations. Penetration of foliage, nets, and ground cover is also possible [33].

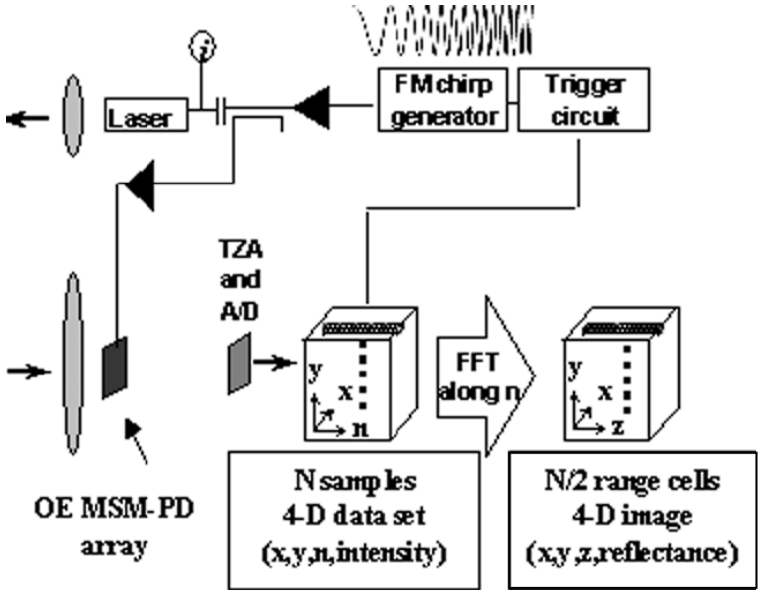

Figure 2-26: FMCW setup; from [33]

The AM laser light (RF) is detected by a 1x32 metal-semiconductor-metal photo-detector (MSM-PD) array in Figure 2-25. The local oscillator (LO) voltage is applied directly to the MSM-PD in Figure 2-24. The RF and LO voltage signals are then mixed

to produce intermediate frequency (IF) signal accomplished by modulating the detector's responsively. The detectors were measured with LO frequencies of up to 800 MHz.

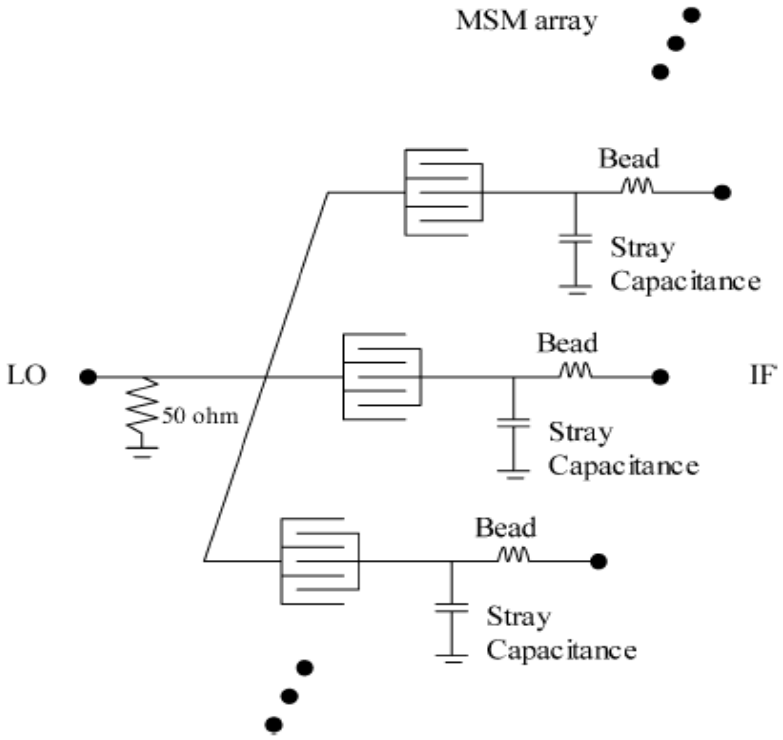

Figure 2-27: MSM-PD fan-out array circuit schematic; from [33]

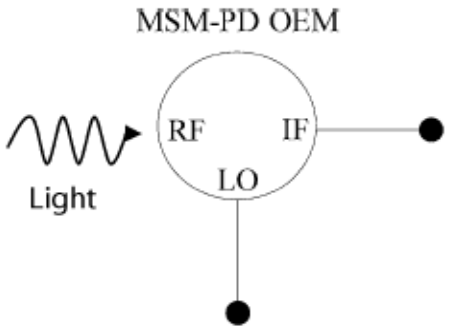

Figure 2-28: Basic model of MSM-PD; from [33]

The MSM detectors play the role of optical receivers. The detectors are used in the breadboard LADAR for high-speed LADAR imaging which eliminates the need for wideband trans-impedance amplifiers in LADAR receiver. The focal plane is composed of a linear array of 32 MSM detectors. Common properties for each detector include:

- Ti/Au (500 angs./4000 angs.) Schottky contacts
- 3 μm wide metalized fingers deposited on Ti/Au substrate
- 5-um wide inter-electrode spacing
- Active area of 250 x 250 μm^2

The overall array size is 8 mm x 0.25 mm. DC characteristics of the detector elements behave similarly to single element MSM detectors previously reported by Ruff, *et al* [33].

Deddis, *et al.*, implemented an inverted metal-semiconductor-metal (I-MSM) in the design of a 3-D bidirectional optical link with a single-fiber bidirectional communication realization. The optical link was designed to operate as a half-duplex link [9].

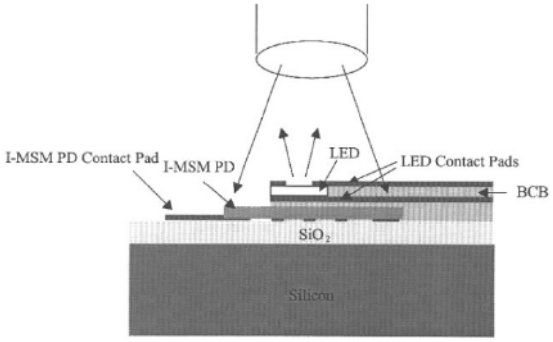

Figure 2-29: 3-D stacking of an independently grown GaAs-based emitter and InP-based detector; from [9]

The I-MSM PD is reported to have higher responsivities relative to the MSM PD [9]. The growth substrate is removed and the finger shadowing is eliminated with the I-HMSM PD implementation (see Figure 2-26). In Figure 2-27, the light-emitting diode (LED) and PD is bonded to a nitride-coated Si host substrate and the Schottky contacts are Pt-Ti-Pt-Au. Device properties include a 5 μm LED diameter and a 200 μm I-MSM PD diameter [9].

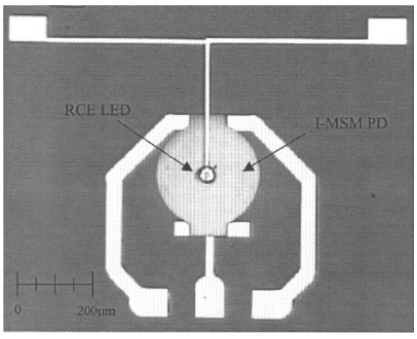

Figure 2-30: Co-located thin-film, GaAs LED InGaAs I-MSM PD stacked device; from [9]

The co-location method has minimal effect on I-MSM PD dark-current characteristics and the I-MSM responsively is smaller (0.31 A/W) than the I-MSM responsively (0.36 A/W) without LED integration; the PD is shadowed by the LED [9].

A wideband preamplifier was fabricated and heterogeneously integrated with an I-MSM PD for a trans-impedance amplifier / photo-detector post-integration [38]. Figure 2-28 gives the layout of the trans-impedance amplifier / I-MSM PD. An externally modulated optical signal (λ_o = 1.55 μm) was launched through a single mode lensed fiber that was vertically coupled into the photo-detector. The integrated circuit was mounted on a printed circuit board (PCB) for biasing with the following PD properties:

- 20 um diameter InGaAs thin film PD
- Responsively of 0.15 A/W
- λ=1.55 μm

With this configuration, the parasitic inductance is minimized which eliminates the need for bonding wire [38].

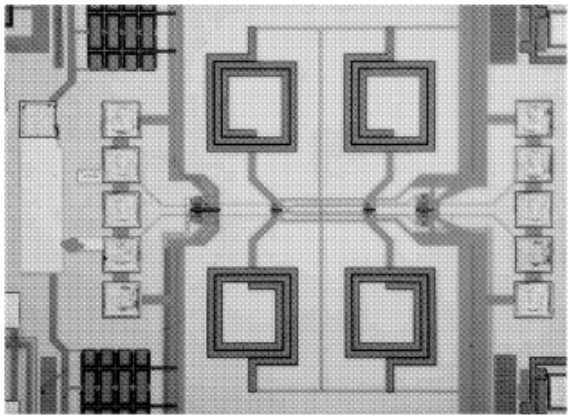

Figure 2-31: Layout of trans-impedance amplifier / I-HMSM PD; from [38]

The Packaging Research Center at the Georgia Institute of Technology designed a fully embedded optical interconnection on PWBs; a thin film I-MSM PD embedded in the core layer of the channel waveguide on a planarized PWB with dimensions of 150 μm X 300 μm in area and is approximately 1 μm thick [38].

In experimental results reported by the Packaging Research Center, the photocurrent increased as applied voltage is increased and saturated at approximately 1V. The amplitude of the photocurrent is more than 100 times larger than dark current at 5V. After applying an impulse input with a full width / half maximum (FWHM) of 500fs, an FWHM impulse response was 22 ps with a responsively of 0.64 A/W. These results proved the embedded photo-detector and the waveguide were functional [39].

Using inter-digitated fingers as seen in Figure 2-29, the Institute of Ion Beam Physics and Materials Research designed an impulsive generator of terahertz radiation. The MSM structure is modified to achieve unidirectional carrier acceleration. The inter-digitated electrode MSM structure is masked by a second metallization layer that is isolated from MSM electrodes and the optical excitation of the MSM structure is blocked

every second period. Thus, the electric fields interfere constructively in the far field with field amplitudes up to 85 V/cm [10].

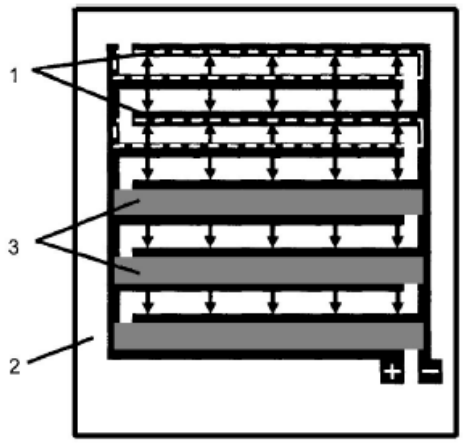

Figure 2-32: Inter-digitated electrode MSM structure; from [10]
1) **inter-digitated electrodes with 5μm spacing**
2) **semi-insulated GaAs substrate**
3) **opaque metallization shadowing a single electric field direction (field direction indicated by arrows)**

As reported by Dreyhaupt, *et. al*., [10] the impulsive generator has the following properties:

- 50 fs, λ=800 nm beam with a repetition rate of 78 MHz is used for excitation
- Excitation density = $1.7 \times 10^{18}/cm^3$
- 15% duty cycle of 50 KHz square wave bias voltage
- THz E-field maximum increases linearly with an increasing acceleration

An MSM-based integrated CMOS wavelength tunable optical receiver with 1 ns switching access time is demonstrated by Chen, *et al.* [5]. In this device, a beam is interfered with a delayed version of itself represented as a dashed and solid sine wave, respectively, in Figure 2-30. The delayed signal is generated by the setup in Figure 2-31. The two electrodes Region I & II are biased with equal but opposite polarity, and the net photocurrent is collected from the desired wavelength thus canceling the undesired wavelength. Channel spacing and wave length is defined as λ_{eff} and λ, respectively, in Figure 2-31. The angle θ of the interfering beams dictate the pattern's spatial period which should match the switching period *w* of device. Wavelength reconfiguration speed is essentially limited only by the switching times for biasing patterns. Figure 2-32 shows the schematic layout of the CMOS receiver [5].

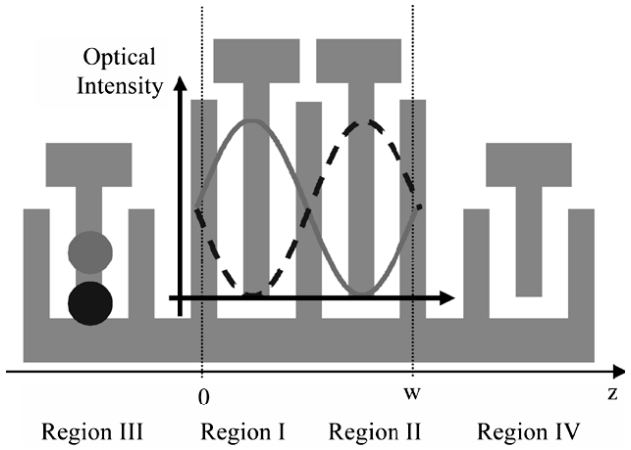

Figure 2-33: Tunable MSM device with two wavelength channels; from [5]

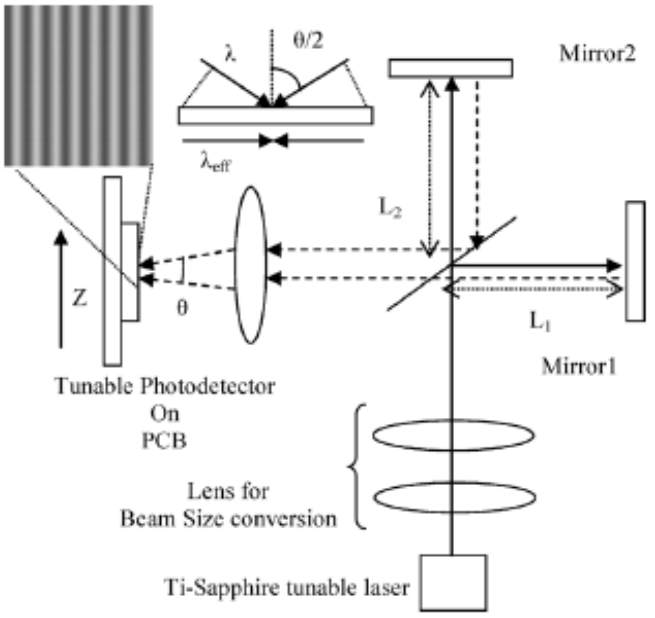

Figure 2-34: Michelson interferometer to generate two beams with an optical path length difference; from [5]

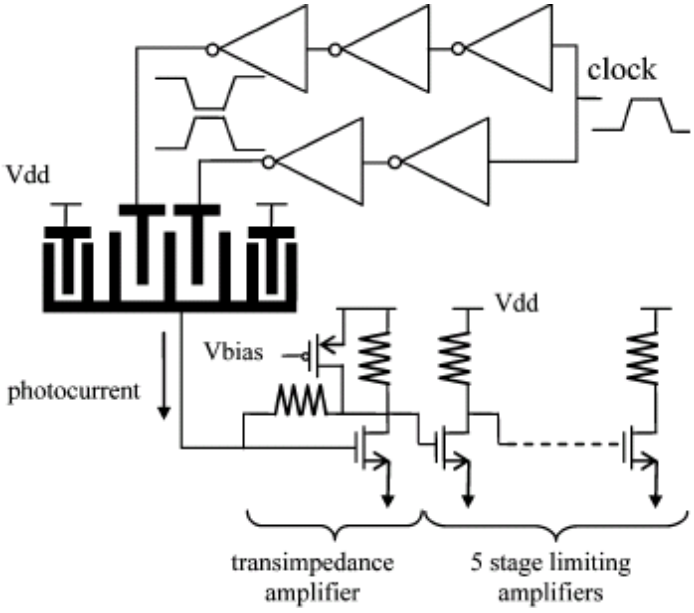

Figure 2-35: Schematic of the CMOS tunable optical receiver and detector driver; from [5]

3. Electron Beam Induced Current Method

3.1. EBIC Background

The electron beam-induced current (EBIC) method is a semiconductor analysis technique that employs an electron beam to induce a current signal within a sample which is then used to generate images; characteristics of a sample are depicted such as p-n junction locations, local defects, and doping non-homogeneities. An SEM is typically employed in this method since it provides an electron beam source suitable for this purpose. Typically EBIC systems consist of an SEM, an external low-noise current amplifier connected to a high-vacuum electrical feed-through that is electrically connected to a sample located inside the SEM chamber, and a sample holder that has the required electrical contact points to facilitate the electrical sample-to-feed through connection [37].

When an electron beam penetrates a semiconductor, decelerated charge carriers of opposite polarity, or electron-hole pairs, are created with energies near band-gap energy of the host material; one unit charge is induced for each pair in an external circuit. These charge carriers drift in random motion and will eventually recombine or annihilate each other so long as there is no electric field present that is strong enough to separate and collect them. If a localized electric field exists within the semiconductor, it can influence the charge carriers to move in a specific direction; relative to field orientation, holes and electrons will be separated and swept in opposite directions.

Electric fields can exist either through internal p-n junctions, local defects within the semiconductor, or external biasing sources [37].

Electron-hole pair generation by way of an electron beam is also understood to be the pre-stage of cathodoluminescence. Cathodoluminescence is defined as an electrical phenomenon when a beam of electrons generated by an electron gun generates optical effects in a sample; it is the light emission associated with the excitation of materials by an electron. Cathodoluminescence is due to effects of radiative recombination and its contrast is associated with the ratio of radiative to non-radiative processes [37].

By electrically contacting the host semiconductor under EBIC methods, which is typically done with non-rectifying or ohmic contacts, charge carriers can be collected, amplified, and analyzed. In the analysis stage, variations in charge carrier generation, drift, or recombination is interpreted as variations of contrast in an EBIC image. Note that relative to charge carrier generation and drift, EBIC imaging is much more sensitive and responsive to electron-hole recombination. In a localized region of a p-n junction, electron-hole recombination is enhanced which reduces the collected EBIC current in defect areas. Thus, if the current through the junction is used to produce the EBIC image, the areas with physical defects will appear darker in the EBIC image relative to areas without any physical defects. Such locations act as recombination centers. Therefore EBIC imaging is a suitable tool for finding sub-surface and other embedded damage locations which give reason to why the EBIC method is used in locating defects in semiconducting material. It is important to know that

cathodoluminescence and EBIC signaling are mutually exclusive processes for each electron-hole pair generated in any device [29] [37].

A simple EBIC relation for the electron beam induced current I_{EBIC} is given as:

$$I_{EBIC} = I_B \cdot \left(\frac{E_B}{E_{e\text{-}h}} \right) \cdot \Sigma , \tag{12}$$

where E_B being the primary beam energy (also given as the accelerating voltage multiplied by q), and $E_{e\text{-}h}$ being the energy needed to create an electron-hole pair. Assuming an ideal collection efficiency of 100%, an electron beam energy of 20keV (typical), and electron-hole generation energy of 1.42 eV (typical for GaAs), the EBIC current is approximately three orders of magnitude larger than beam current as stated above; $I_{EBIC}/I_B >> 1$. In other words, with I_B in the range of pico-amps, I_{EBIC} is in the ideal range of nano-amps to a few micro-amps [37].

3.2. EBIC Method Applications

Applications of EBIC method analysis include the following:

- Detection of crystal lattice defects
- Detection of semiconductor pipes
- Detection of extra junctions or doping layers
- Identification of ESD/EOS failures sites

- Measurement of depletion layer widths and minority carrier diffusion lengths/lifetimes.

Crystal lattice defect detection is represented as dark spots or lines in an SEM image. Collector pipes result in collector-emitter leakage currents in bipolar transistors. Electrostatic discharge (ESD) is a transfer of electrostatic charge between bodies or surfaces at different electrostatic potentials, either through direct contact or through induced electrical fields. Electrical overstress (EOS) is a thermal overstress event introduced when a product is exposed to a current or voltage beyond its maximum rating, usually from power supplies or test equipment [37].

4. Theoretical Study with EBIC Method and Degenerate Devices

4.1. Scanning Electron Microscope Beam Energy Control

The EBIC system includes an external biasing circuit which monitors the current passing through the test devices in a scanning electron microscope. The SEM is used to provide the electron beam source with approximate beam energies between 500 eV to 30 KeV. With the minimum energy of the SEM's electron beam being much greater than the energy needed to produce cathodoluminescence or even induce current within GaAs, the electron beam penetration depth can be used to control the beam energy that reaches the electron or hole gas embedded in degenerate in-plane Schottky contact or HMSM devices.

Das, *et al.,* investigated the beam energy effect on the mobility of a two-dimensional electron gas for the structure in Figure 4-1 [8]. During electron beam exposure, the primary electron beam lost energy in the test device as it passed through the semiconductor medium. For Das', *et al.*, experiment, the distribution of the energy loss as a function of penetration depth (dE/dz) was determined as:

$$\frac{dE}{dz} = 10^3 \cdot \frac{E_o}{R_G} \cdot \left(P_o(z') - 0.57 \cdot P_1(z') - 0.53 \cdot P_2(z') + 0.28 \cdot P_3(z') \right), \qquad (13)$$

where E_o is the initial beam energy in eV, the penetration distance (z') is given by

$$z' = \frac{2 \cdot z}{R_G}, \tag{14}$$

the maximum range of the electron beam inside the medium, the Gruen range (R_G), is given by

$$R_G = \left(\frac{4.28 \times 10^{-6}}{\rho} \right) E_o^{1.75}, \tag{15}$$

where ρ is the density of the medium, and P_0, P_1, P_2, P_3 are the shifted Legendre polynomials, respectively. By observing the decrease in electron mobility due to the causal electron-beam perturbation effects, it was postulated that at beam energies above 15 keV the interaction volume reached deep into the sample with minimal two-dimensional sheet charge interaction. Referring to Figure 4-2, dE/dz is low enough in the sample where a decrease in charge mobility is not detectable [4].

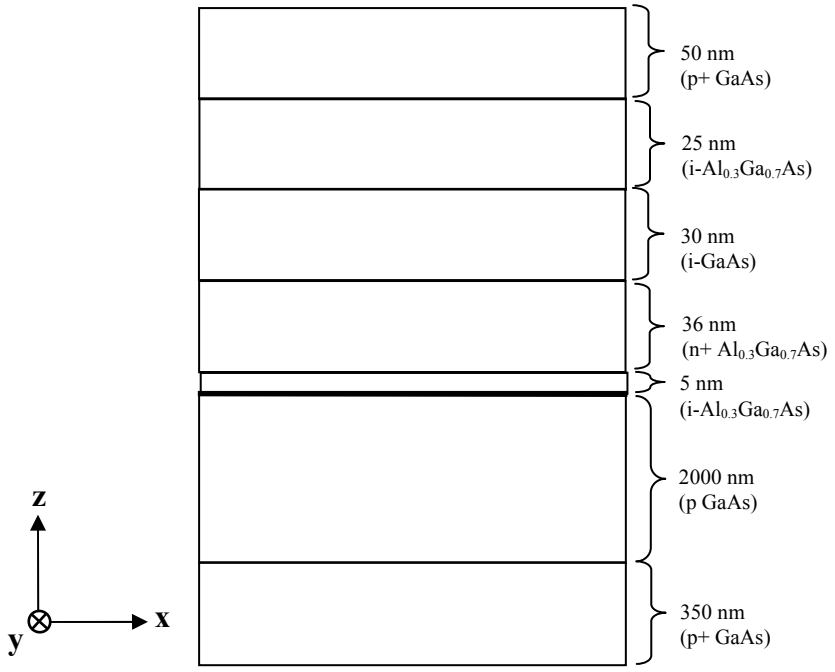

Figure 4-1: Cross-sectional diagram of structure used in [8]

The electric field in the space charge region is also determined from Poisson's ideal, one-dimensional equation and is given as:

$$\frac{dE}{dz} = \frac{\rho(z)}{\varepsilon_s}, \tag{16}$$

where $\rho(z)$ is the charge density and ε_s is the permittivity of the semiconductor.

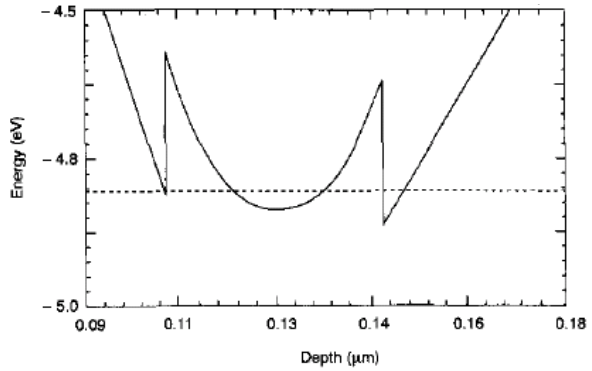

Figure 4-2: Conduction band simulation of structure near 2DEG used in [8]

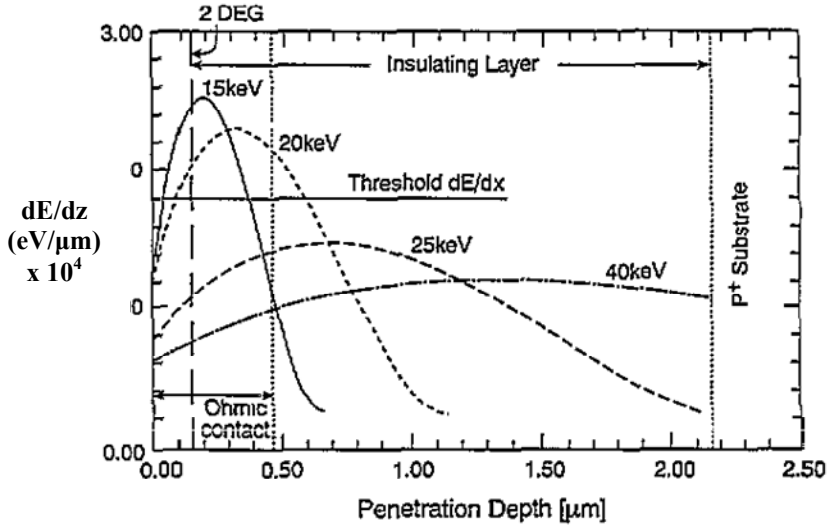

Figure 4-3: Theoretical dE/dz Vs. penetration depth at different beam energies in [8]

Figure 4-3 illustrates the calculated plot of dE/dz versus penetration depth for different beam energies superimposed on the experimental structure of Das, *et al.* The 2DEG location is shown to penetrate to 0.15 μm within the GaAs substrate. Threshold dE/dz is the level below which there is no measurable effect of the electron-beam damage [8].

Using the formulated equations, the energy at the GaAs surface for a particular beam energy E can be calculated using

$$-\frac{dE}{dz} = 2\pi \cdot N_A \cdot e^4 \cdot \left(\frac{Z \cdot \rho_{mean}}{A}\right) \cdot \frac{1}{E} \cdot \ln\left(\frac{E}{I} \cdot \sqrt{\frac{e}{2}}\right), \tag{17}$$

where *I* is defined as

$$I = Z \cdot \left(9.76 + 58.8^{-1.19}\right) \tag{18}$$

Here N_A, Z, ρ_{mean}, and A are Avogadro's number, the average atomic number, the mean density, and the atomic weight of the medium, respectively [8].

These equations were used to estimate the effective energy of the beam after it pass through a 1.5 μm thick PMMA layer; the energy of the electron beam is completely dissipated in the resist for beam energies up to 10 keV in the Das, *et al.,* experiment [8].

Based on the findings of Das', *et al.* experiment [8], knowing and manipulating the energy of the electron beam at the degenerate AlGaAs/GaAs interface, in theory, can be used to sweep the generated electron-hole pairs with maximum efficiency; the current path used in EBIC detection is minimized for charge carriers generated near the interface plane with energies comparable to local equilibrium majority carriers thus minimizing scattering affects.

4.2. Electron-Electron Scattering

Electron-electron scattering is understood to be the dominant interaction between a two-dimensional electron gas and an electron-beam. Gurzhi, *et al.* described the modified one-collision approximation to explain the equilibrium electron/non-equilibrium electron interaction. The spectroscopy method was used to determine the energy and angle dependence of electron-electron scattering in a two-dimensional electron gas in a very direct manner; recent theoretical computations and experimental results agreed to a great extent; the differences in electron-electron scattering in a two-dimensional system relative to a three-dimensional system were exposed. Most notably is the increased importance of small-angle scattering in a two-dimensional system. Due to small-angle scattering, a reduced broadening of the electron beam resulted [14].

For electron-electron scattering, focus is placed on the high-energy beams with typical electron energy that exceeds the thermal energy of the equilibrium electrons within the 2DEG that are significantly below the Fermi energy. This is where small-angle scattering events dominate and the scattered electrons may remain within the region of the electron beam [15].

According to Fink, *et al*., there are two types of electron-electron collisions with nearly the same probability characterize scattering in 2D systems; equilibrium/non-equilibrium collisions and equal but opposite momentum electron-electron collisions. Collisions of a non-equilibrium electron with momentum $\mathbf{p}$ and excess energy $\boldsymbol{\varepsilon}$ with equilibrium electrons of momentum $\mathbf{p_1}$ usually result in scattering of both electrons by a small angle $\psi \sim \varepsilon/\varepsilon_F$, where ε_F is the Fermi level energy. The $\mathbf{p}$ and $\mathbf{p_1}$ states scatter into

states $\mathbf{p_2}$ and $\mathbf{p_3}$ and leaves an empty space in the Fermi distribution in the state $\mathbf{p_1}$, otherwise referred to as a hole, thus $\mathbf{p} + \mathbf{p_1} = \mathbf{p_2} + \mathbf{p_3}$. [15] In the case of collisions with electrons of nearly opposite momentum, ($\mathbf{p} \sim -\mathbf{p_1}$), the electrons at $\mathbf{p_2}$ and $\mathbf{p_3} \approx -\mathbf{p_2}$ are scattered by a much larger arbitrary angle ψ; on average $\psi \approx \sqrt{\varepsilon/\varepsilon_F}$ [15].

According to the experimental data conducted by Gurzhi, *et al*. [14], there are two types of electron-electron scattering events to consider within an electron cloud; a case where a few collisions occur and a case where collisions occur frequently. In the case of a few electron-electron collisions an electron has a small scattering probability to be detected traveling the distance between the injector and detector (L) as indicated in Figure 4-4; the electron-electron mean-free path (l) is much greater than the characteristic length L ($l >> L$) [14]. Perturbation theory can then be used to solve the Boltzmann equation by iteration of the collision operator [15]. A hydrodynamic situation arises in the case of frequent electron-electron collision.

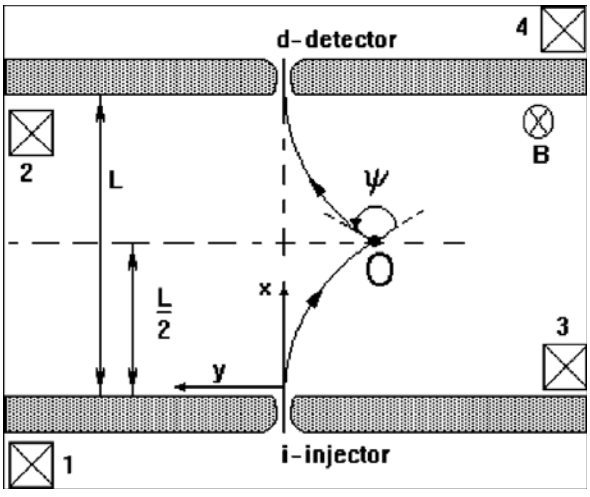

Figure 4-4: Schematic top-view of the device layout used in [15]

The hatched areas in Figure 4-4 are Schottky gates defining the device geometry. The crossed squares denote the ohmic contacts and the i-injector and d-injector symbolizes the injector and detector of the quantum point-contact, respectively.

Gurzhi, *et al.,* discusses their approach to explaining the intermediate case where l is proportional to $\boldsymbol{L}$ and the scattering probability substantially decreases with each collision. In their approach, otherwise known as the modified one-collision approximation, the few electron-electron collisions are treated as above but the frequent collisions are perturbationally considered [14].

4.2.1. Modified One-Collision Approximation

The modified one-collision method is a theoretical approach for the electron beam propagation in small systems. High energy, non-equilibrium electrons at a characteristic energy ε that is measured from the Fermi level energy ε_F and larger than the equilibrium energy of the electron gas kT, are scattered by the equilibrium electrons in the first stage of relaxation. A new non-equilibrium system is generated and has lower excess energy than the initial non-equilibrium electrons; this stage is otherwise known as the pre-temperature stage. The probability of secondary collisions is an order of magnitude lower than initial collisions [14]. The premature stage ends when the quasi-particles' energy approaches the equilibrium energy kT; after the non-equilibrium/equilibrium electron collision, the energy of the non-equilibrium electron will be distributed accordingly.

$$\mathbf{p + p' \rightarrow p'' + p'''} \tag{19}$$

or similarly in energy form,

$$\varepsilon_o = |\varepsilon'| + \varepsilon'' + \varepsilon''' \tag{20}$$

For $kT << \varepsilon_o$, the energy of an incident electron ε_o is redistributed between three final stages, $\varepsilon' < 0$ (hole left in 2DEG), and ε'', $\varepsilon''' > 0$. The Pauli Principle predicts that state **p'** will be below the Fermi level and the final states **p''** and **p'''** are well above the Fermi Level. As a function of energy, the mean-free path $l(\varepsilon)$ is proportional to $1/\varepsilon^2$ [15]. Thus the mean-free path of the equilibrium ε' is greater than the non-equilibrium ε_o; $l(\varepsilon') >> l(\varepsilon_o)$. In essence, the probability of the first collision is near unity in a system of size L while the probability of the second collision is relatively low [14].

Fink, *et al.*, showed that there exists a maximum peak in mobility degradation in the two-dimensional electron gas of approximately 13% (see Figure 4-5) upon electron perturbation [12]. Charged defects created in proportion to dE/dz can explain the energy dependence of mobility degradation. It is postulated that at higher beam energies, dE/dz is low enough in the region of the 2DEG, and the high damage region or beam penetration volume is sufficiently remote from the 2DEG, so as not to create enough defects to have a measurable effect on the mobility [12].

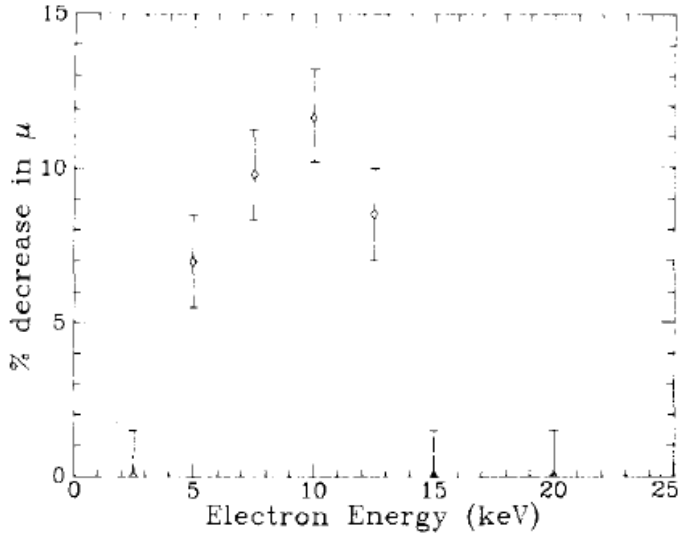

Figure 4-5: Percentage mobility degradation vs. electron energy used in [12]

4.3. Biased in-plane Schottky contact device under E-beam perturbation

The device layouts for non-degenerate and degenerate, biased in-plane Schottky contact devices under electron-beam perturbation are given in Figure 4-6 and Figure 4-7, respectively, directly above depletion region. Due to the modulation doping for the degenerate device, a vertical electric field exist which sweeps charge carriers to the two-dimensional gas. This vertical field does not exist for the non-degenerate device; a horizontal field pushes charge carriers through the device from contact to contact at a characteristic drift speed.

Electron-hole pairs generated near or in the depletion region are swept and detected by the external EBIC circuit for both types of devices. A major difference in external charge detection is by the manner in which charge carriers are swept through the

device to reach the forward biased junction electrode. The path which the carriers travel in the device can have an affect on the speed at which they are detected.

4.3.1. E-beam Perturbation above Depletion Region

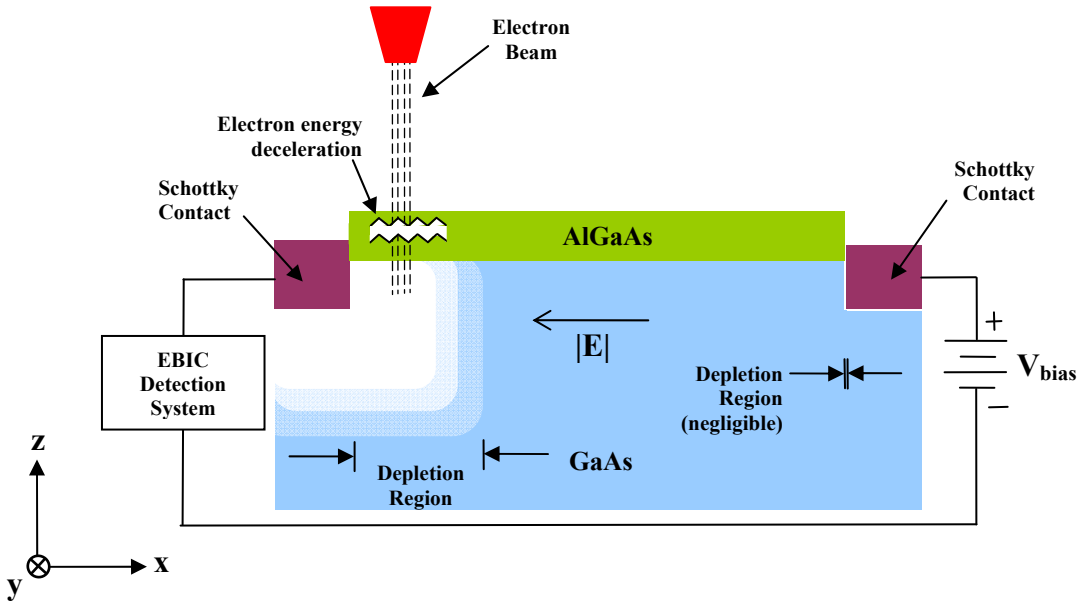

Figure 4-6: Non-degenerate doped in-plane Schottky contact device under bias and electron beam perturbation in depletion region (not-to-scale)

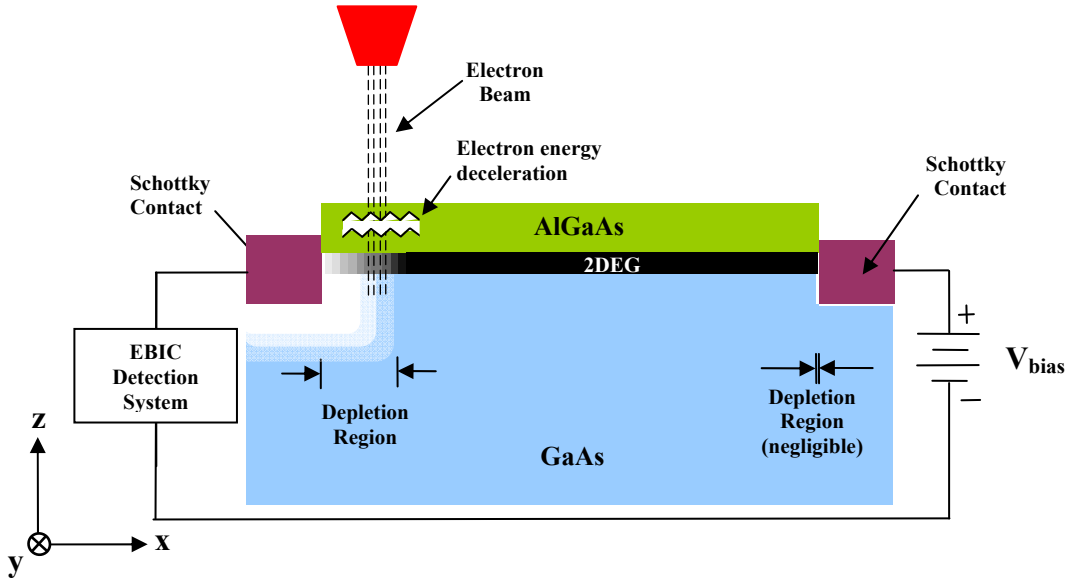

Figure 4-7: Degenerate in-plane Schottky contact/2DEG device under bias and electron beam perturbation in depletion region (not-to-scale)

Figure 4-8 is an illustration of a non-degenerate, biased in-plane Schottky contact device energy band diagram where generated electron-hole pair charge carriers are swept. Figure 4-9 illustrates a degenerate, biased in-plane Schottky contact/2DEG device energy band diagram where charge carriers are swept near the depletion region. Note the applied bias is dropped mostly across the depletion region at the reverse biased junction of the device and not the two-dimensional gas. Relative to the non-degenerate, biased device, the depletion region in the biased degenerate device is stronger and more efficient in sweeping charge carriers to the forward biased junction under similar electron irradiation energy conditions due to its higher electric field.

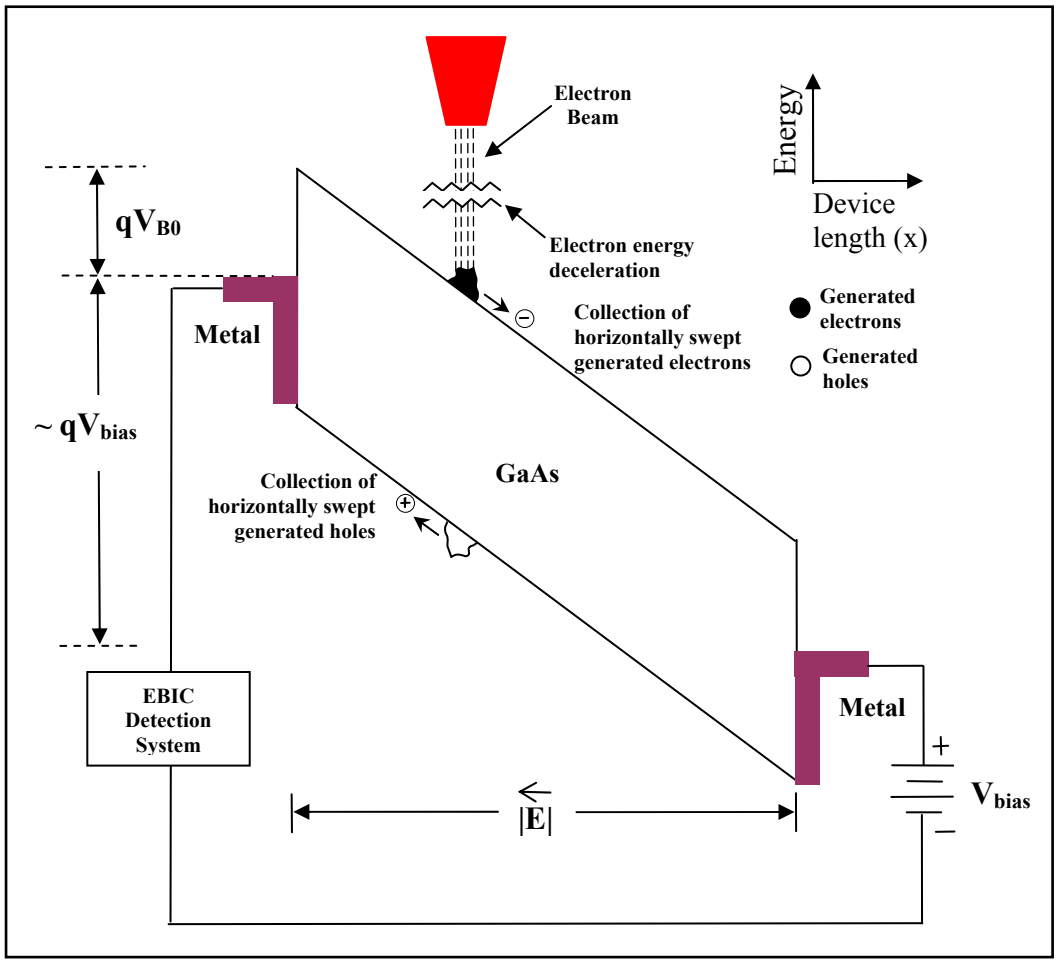

Figure 4-8: Non-degenerate in-plane Schottky contact energy band diagram under bias and electron beam perturbation ($|V_{bias}| > |V_{FB}|$)

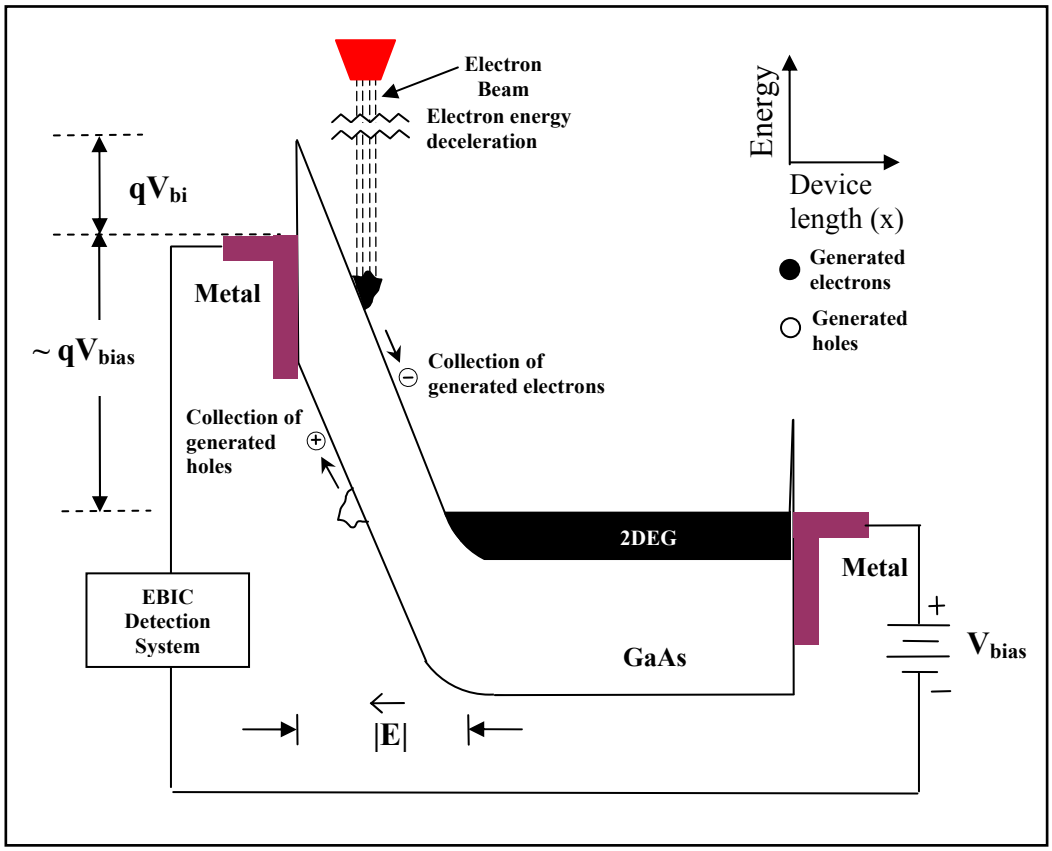

Figure 4-9: Degenerate in-plane Schottky contact/2DEG energy band diagram under bias and electron beam perturbation in depletion region

A degenerate in-plane Schottky contact/2DEG device under electron-beam perturbation is illustrated in Figure 4-10. A depletion region exists for the reverse bias metal-semiconductor interface. Under electron beam perturbation, electron-hole pairs are generated and swept by the vertical electric field that exists underneath the two-dimensional sheet charge; electrons are swept to the two-dimensional gas and the holes are swept to the bottom of the device.

4.3.2. E-beam Perturbation above Two-Dimensional Electron Gas

Figure 4-11 illustrates the typical band bending for the in-plane Schottky contact/2DEG system under electron-beam perturbation. The strong electric field beneath the two-dimensional gas vertically separate and collect the generated electron-hole pairs to the electron gas which is held to the same potential as the forward biased metal contact. Charge carriers will then drift to the metal contacts and be detected by the external EBIC system.

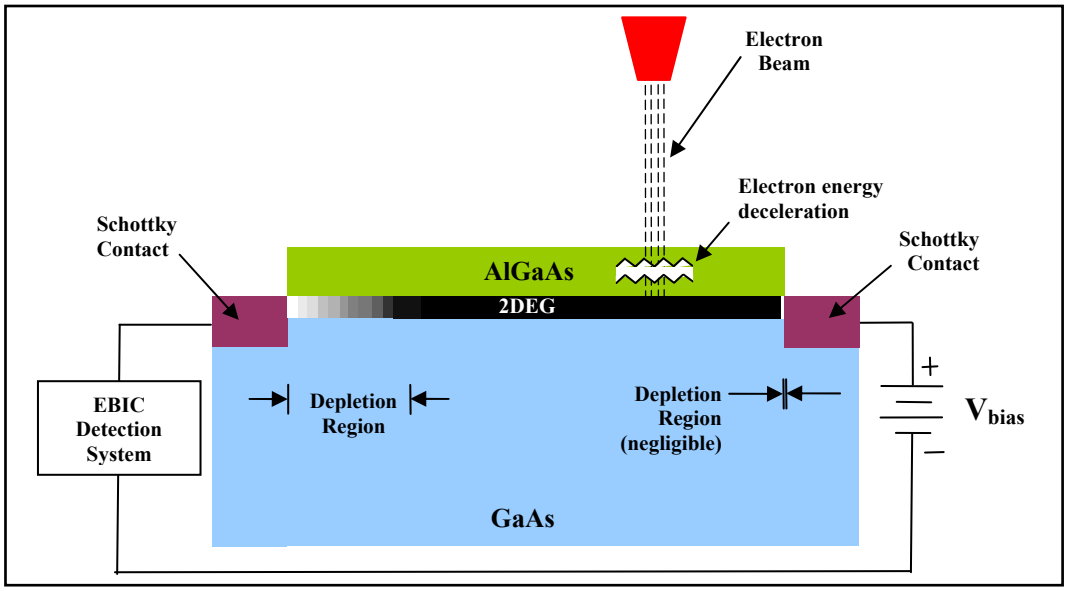

Figure 4-10: Degenerate HMSM device under bias and E-beam perturbation above 2DEG region (not-to-scale)

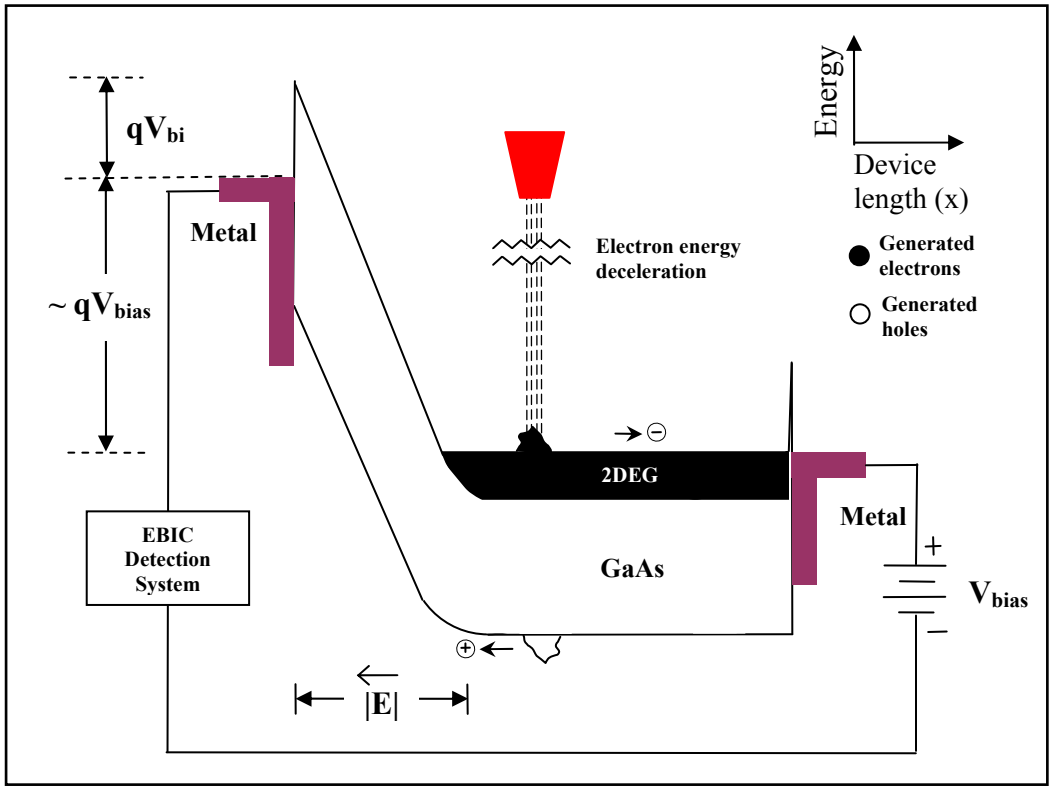

Figure 4-11: Degenerate in-plane Schottky contact/2DEG energy band diagram under bias and e-beam perturbation in 2DEG Region (not-to-scale)

4.4. Biased HMSM device under E-beam perturbation

Due to the depletion region residing below the reverse biased junction electrode of the HMSM device, the electron beam has to be focused as close to the this electrode as possible to approach maximum EBIC effectiveness from the depletion region upon the perturbing electrons; high beam reflectance will result when focusing the electron beam directly above either electrode.

In previous simulations of delta modulation doped HMSM devices, it is predicted there exist a vertical electric field within the device's active region just below the reverse biased junction electrode. Similar to the undoped device, the depletion region is where most of the external biasing potential is dropped. The depletion region under the reverse biased junction electrode has a vertical field sweeping electrons to the bottom of the device. With the 2DEG sheet charge shielding the bulk material directly below from any lateral electrical fields, there exists another vertical field that sweeps electrons toward the 2DEG sheet charge thus taking full advantage of the confined electron sheet by way of electron detection. [45]

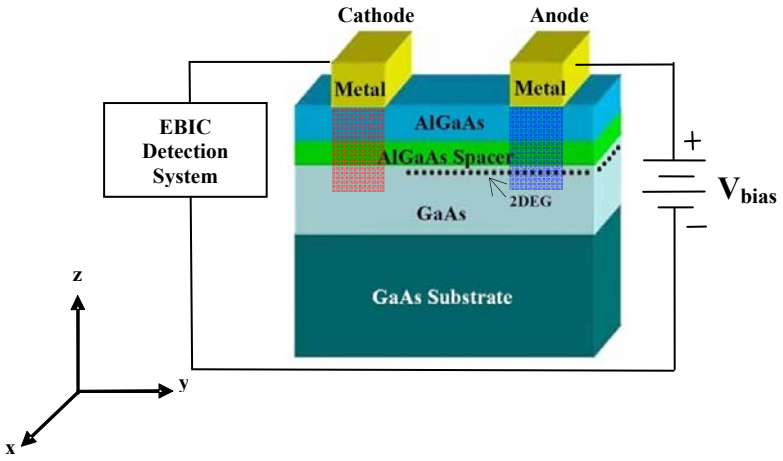

Figure 4-12: 3-D illustration of degenerate HMSM device under bias [45]

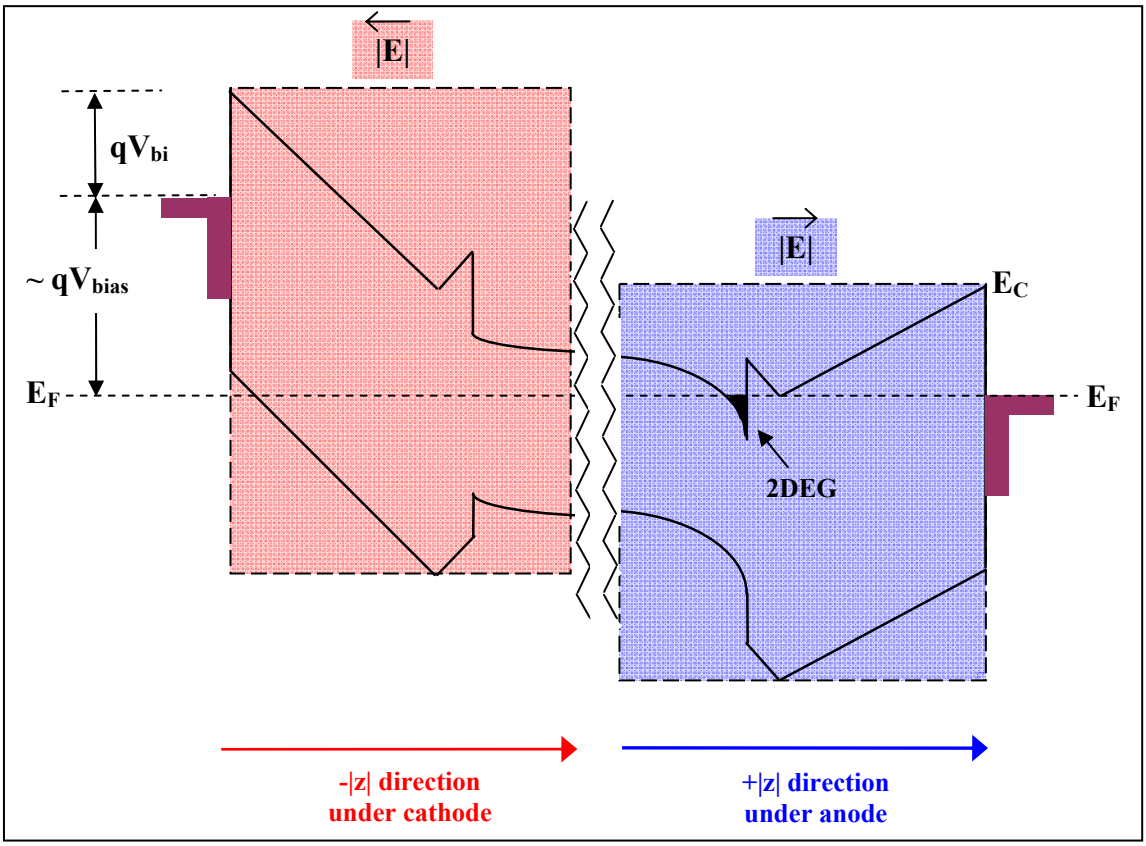

Figure 4-13: Degenerate HMSM energy band diagram under bias

4.4.1. E-Beam Perturbation Near Depletion Region

At higher biasing levels, a depletion region can exist near the reverse biased junction electrode of the degenerate device upon which the vertical electric field separates generated electron-hole pairs. This strong vertical electric field sweeps the electrons to the bottom of the active region and the holes to the cathode. At the bottom of the active region, a horizontal electric field moves the electrons toward a strong shielding vertical field that sweeps the electrons to the 2DEG sheet charge (see Figure 5-9).

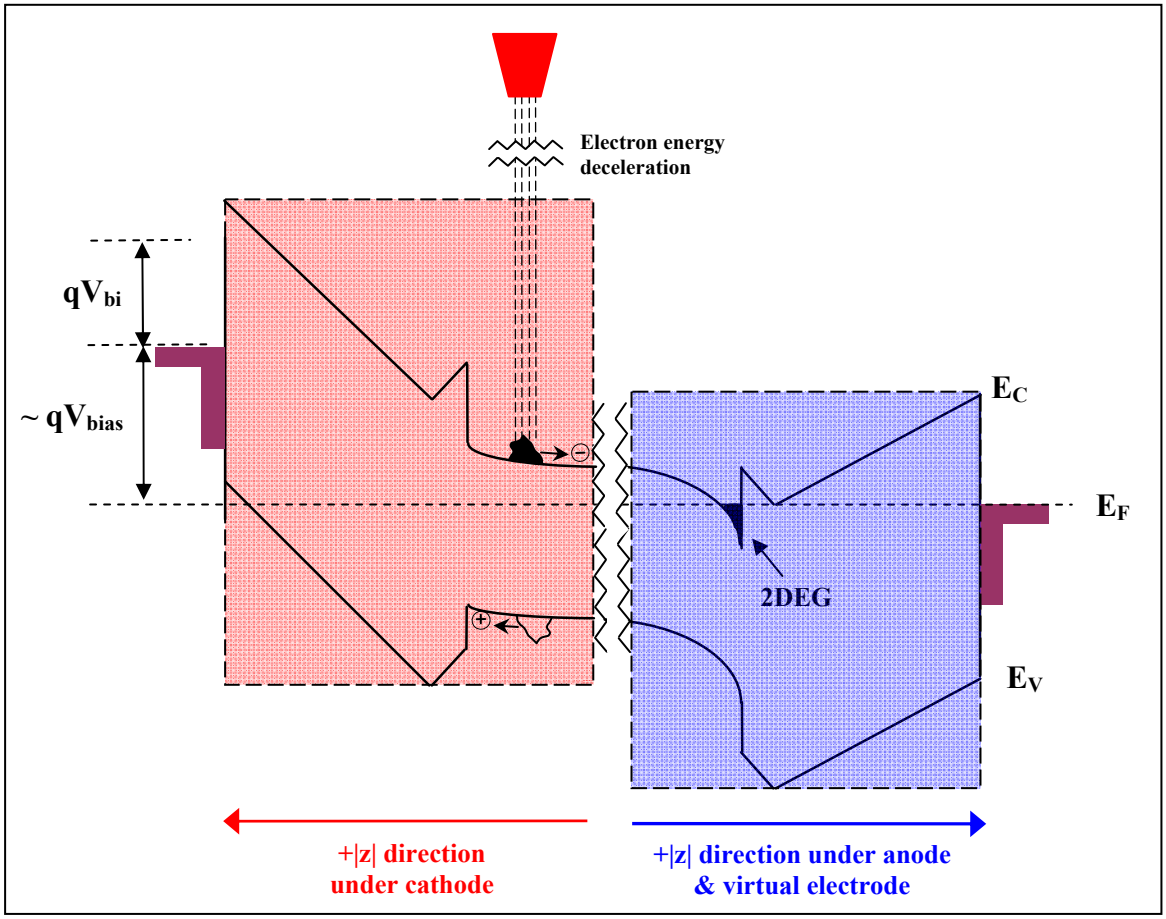

Figure 4-14: Degenerate HMSM energy band diagram under bias and electron beam perturbation near cathode

4.4.2. Below Two-Dimensional Electron Gas

As stated in the previous paragraph, at the bottom of the active region, a horizontal electric field moves the electrons toward a strong vertical field that sweeps the electrons to the 2DEG sheet charge. Electrons that reach the two-dimensional sheet charge are collected at the anode producing an external current.

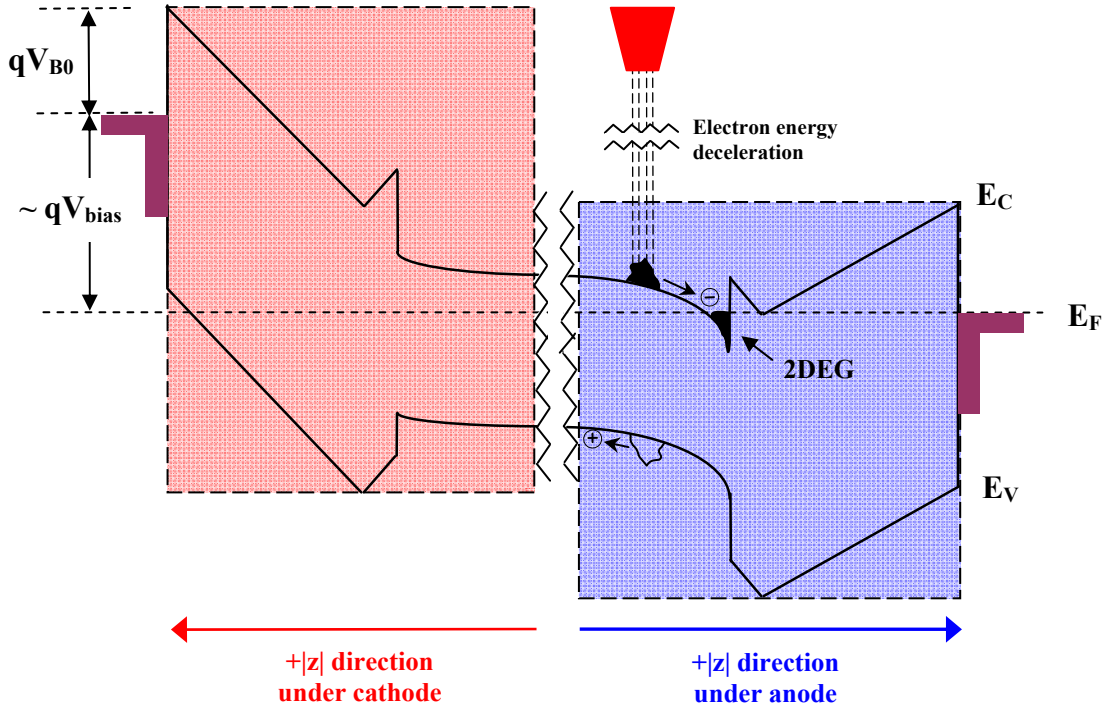

Figure 4-15: Degenerate HMSM energy band diagram under bias and electron beam perturbation in depletion region

4.5. Theoretical Discussion of Electron-Electron Scattering

If two electron energy states with higher energy than that of an equilibrium electron is the end result of a non-equilibrium-equilibrium electron scattering event, one can conclude that the density of the two-dimensional electron gas is effectively degraded for every such event. As the density of the 2DEG degrade so does the degenerate doping level of the host semiconductor and it is hypothesized that lattice defects are created due to this electron-electron scattering [6]; current density within the MSM device is lowered and is observed in the EBIC signal as a reduction in current. This theoretical summation is only valid if the beam interaction volume's maximum spread is intersecting the 2DEG sheet charge. Otherwise, electron-electron scattering has minimal effect on device current flow.

5. Discussion of Experimental Results

The test device I-V characterization data results were not produced using the circuit design presented earlier; thanks to IME-CNR of Lecce, Italy, the experimental results presented and analyzed here stand alone. In reference to the trans-impedance amplifier circuit design, the EBIC circuit can be used as a base-point in developing a circuit prototype for future use.

As mentioned in section 2.3.2, two types of devices were made readily available by CNR/IMM for EBIC testing; undoped and delta-doped hole-gas (2DHG) HMSM devices. Note that using 2DHG as opposed to 2DEG devices does not change the principle ideas of this thesis study. Remembering that the perturbing electrons generate electron-hole pairs that are swept relative to the electric field is independent of modulation doping type; major device-specific affect is device current speeds. Thus the fundamental principles for the EBIC method using 2DEG and 2DHG devices are the same. Also, by definition the anode/cathode references made earlier for the 2DEG device does not hold for the 2DHG test device; the roles of anode and cathode are reversed.

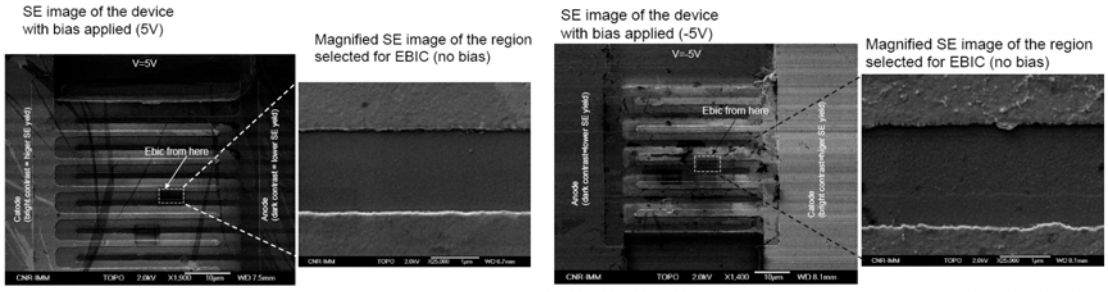

Figure 5-1: SEM images of delta-doped HMSM devices (images courtesy of CNR\IMM, Lecce, Italy)

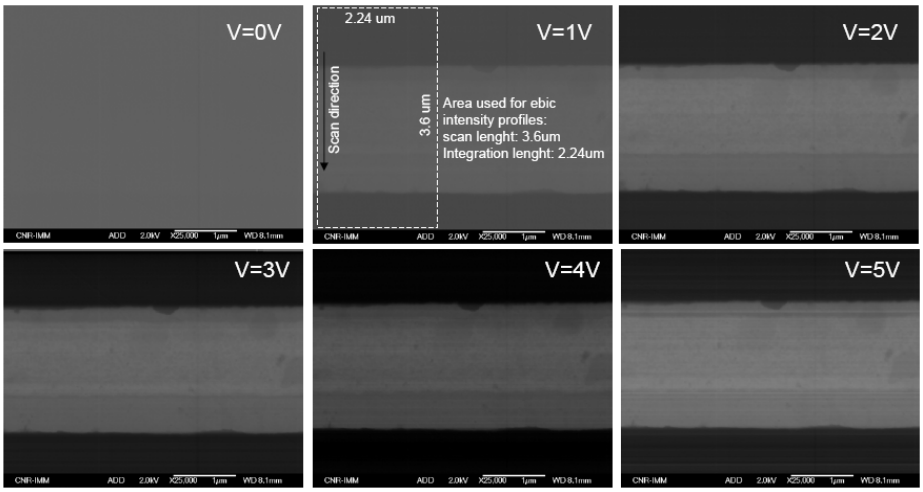

Figure 5-2: EBIC images of HMSM structure (images courtesy of CNR\IMM, Lecce, Italy)

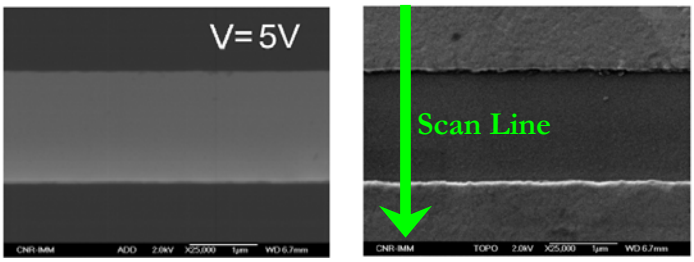

Figure 5-3: EBIC image (5V) & SE image of undoped HMSM structure with scan line path used for EBIC plotting (images courtesy of CNR\IMM, Lecce, Italy)

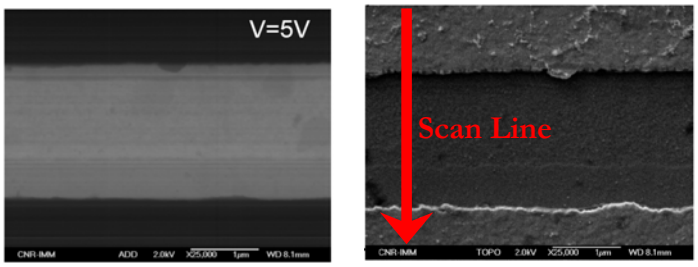

Figure 5-4: EBIC image (5V) & SE image of delta-doped HMSM structure with scan line path used for EBIC plotting (images courtesy of CNR\IMM, Lecce, Italy)

Figure 5-5 and Figure 5-6 is a plot of EBIC device current for five different biasing levels of undoped and degenerate devices, respectively. The EBIC amplifier circuit used to produce these plots is unknown. Fortunately the data has qualitative information that supports this study. Assuming a linear amplification for all reported EBIC signal data, which can be proven with a biasing/dark-current proportionality relationship comparison, it is evident that the degenerate device dark current levels are higher (approximately an order of magnitude) than that of the undoped device current levels with similar biasing. What is not completely clear from these plots is the correlation of the presence of the 2DHG and its affect on device current levels. The simulation results agreed with experimental results revealing a vertical field facilitating the electron transport in the δ-doped MSM structure is more ideal in charge carrier detection.

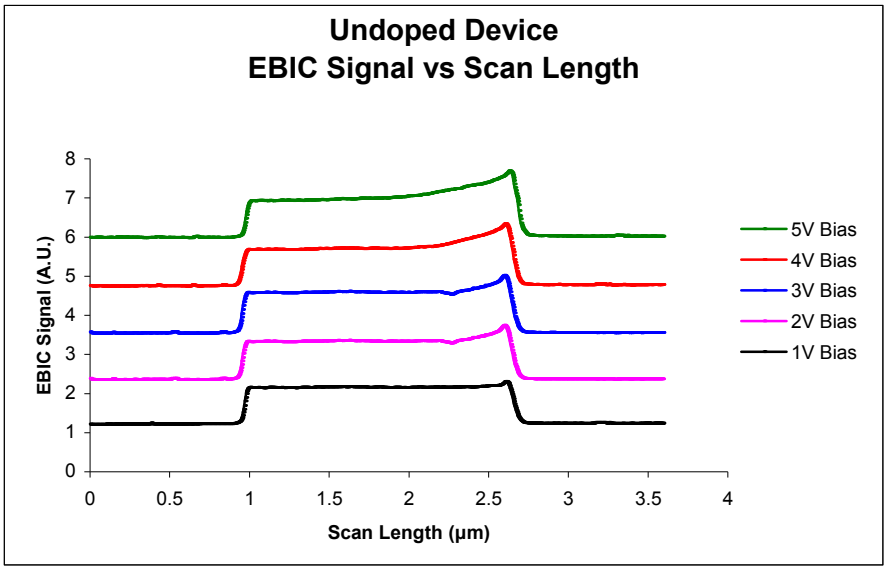

Figure 5-5: Undoped device current vs. scan length at various bias levels (data used to generate plot courtesy of CNR\IMM, Lecce, Italy)

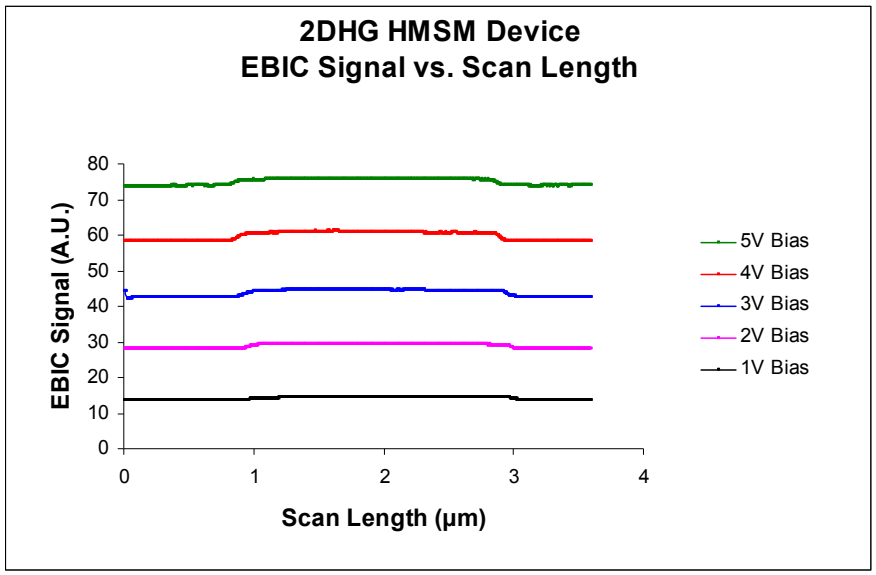

Figure 5-6: Degenerate device current vs. scan length at various bias levels (data used to generate plot courtesy of CNR\IMM, Lecce, Italy)

Be it through charge carrier drift or depletion region sweeping, an important quantitative measurement for the 2DHG test device is the gain in current when the device's active region is optically perturbed. This measurement is the difference between a device's recorded EBIC signal and its signal noise floor. Although the signal gain for each plot is unknown, qualitative purposes allow the need to maintain the given reference values.

After normalizing the noise level for each device, signal-to-noise ratio (SNR) calculation comparisons reveal that the degenerate device's dark currents prove detrimental to its EBIC SNR ratios (see Table V-1 and Table V-2); the undoped device has higher SNR values relative to its degenerate counterpart. From Table V-2, The degenerate device's SNR values are all well below unity, an indication that EBIC signal

extraction is more difficult than that of the undoped device. This is expected since degenerate devices of this type are notorious for higher dark currents. Thus a device's EBIC signal and noise floor are proportionally indistinguishable for the low-biased degenerate device. In Figure 5-11, the current signal for the 5V-biased degenerate device is riddled with noise.

Table 5-1: Undoped device average EBIC and SNR calculations near forward biased junction (data used to generate table courtesy of CNR\IMM, Lecce, Italy)

Bias	Avg. Signal Level (A.U)	Avg. Noise Level (A.U)	SNR (dB)
5V	7.090	5.992	14.61
4V	5.792	4.752	17.19
3V	4.621	3.547	22.98
2V	3.368	2.361	30.88
1V	2.167	1.220	49.89

Table 5-2: 2DHG HMSM device average EBIC and SNR calculations (data used to generate table courtesy of CNR\IMM, Lecce, Italy)

Bias	Avg. Signal Level (A.U)	Avg. Noise Level (A.U)	SNR (dB)
5V	75.668	73.967	0.20
4V	60.751	58.495	0.33
3V	44.432	42.640	0.36
2V	29.360	27.981	0.42
1V	14.378	13.705	0.42

An interesting observation is the undoped device EBIC values near the forward biased junction are kept relatively constant and values near the depletion region increases with an increase in device biasing. This agrees with our previous statement that an increase in external biasing is dropped across the depletion region of the device and not the entire active area. This is not the case for the degenerate device; the EBIC values

appear to be proportional to increased biasing which is dropped across the entire finger-gap or active region. This is due to the sheet charge extending horizontally into device just below the AlGaAs/GaAs interface facilitating the vertical field charge detection. In essence, the presence of the two-dimensional sheet charge replicates a virtual forward biased junction electrode across the top of the device (see Figure 5-7). Unlike the metal contacts, this virtual electrode extension does not suffer from high electron beam reflectivity. Thus the vertical field at the AlGaAs/GaAs interface beneath the virtual electrode mimics that of the vertical field directly below the forward biased junction electrode. Note that in the case of biased HMSM devices, the depletion region is directly beneath the anode in 2DHG devices and beneath the cathode in 2DEG devices.

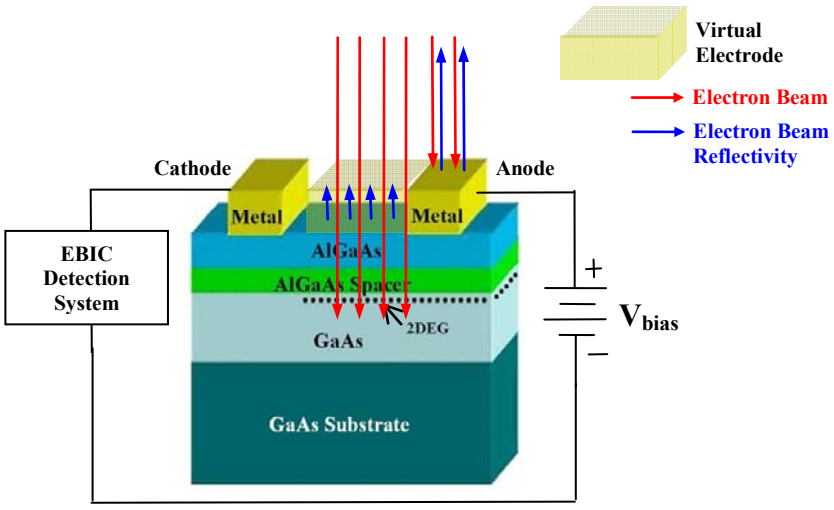

Figure 5-7: Virtual electrode extension effect of two-dimensional sheet charge [45]

Integrated Systems Engineering (ISE) Technology computer-aided design (TCAD) software was used to predict the internal electric field distribution orientation for non-degenerate and degenerate 2DEG HMSM heterostructures (see Figure 5-8 and

Figure 5-9, respectively). The simulation utilizes geometry with finger width of 2-μm, finger gap of 2-μm, and thickness of the active region of 1 μm. The Schottky barrier height is 0.7 V, the contact potential is V_{sc} = -0.7 V at the cathode, and $V_{sa} = V_{bias}$ - 0.7 V at the anode, where, V_{bias} is the externally applied bias [45]. For 2DHG devices, the electric field vectors are reversed in orientation and the strong vertical field would be pulling electrons to the bottom of the device. From the simulated electric field plot in Figure 5-8, the horizontal electric field in the undoped structure's active region sweeps electrons toward the anode to be collected. Characteristic of an undoped device, there exists a constant potential field gradient (dE/dy = 0) in the active region outside the depletion region where limiting drift current can be reached thus impeding charge carrier transport. This potential field gradient is the limiting factor in the collection of charge carriers having near band-gap energy just outside the depletion region. From the plot, the depletion region under the reverse biased junction electrode reaches further into the device as external biasing is increased but has little to no effect on the overall current transport in the active region. The vertical field in the delta-doped 2DEG structure's active region pulls electrons toward the electron gas sheet charge at the AlGaAs/GaAs interface [40].

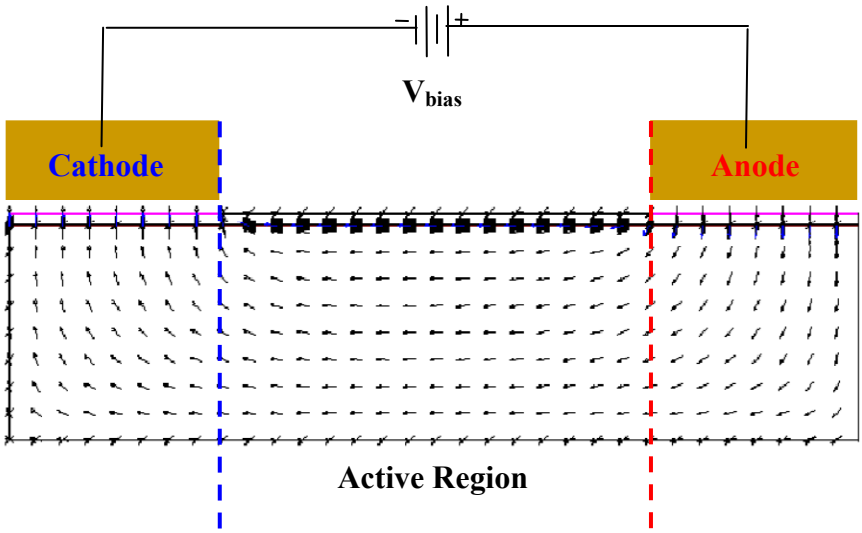

Figure 5-8: Two-dimensional E-field distribution for biased undoped HMSM device [45]

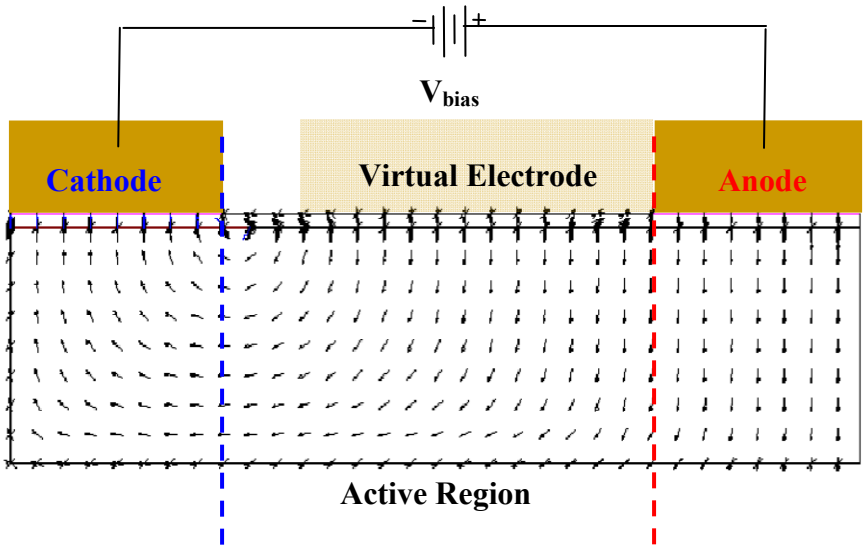

Figure 5-9: Two-dimensional E-field distribution for biased 2DEG HMSM device illustrating virtual electrode [45]

Experimental test results for an undoped HMSM device under five different biasing levels is illustrated in Figure 5-10. Each plot indicates the induced current within

the device under five different biasing levels. The referenced signal floor (zero-reference) is none other than the noise floor for each biasing levels of device. With the undoped device, electrons are traveling at a saturation drift velocity near the forward biased junction electrode. Most of the device biasing is dropped near reverse biased junction electrode [45].

Test results for delta modulation doped 2DHG HMDM device under five different biasing levels is illustrated in Figure 5-11. Each plot indicates the induced current within the device for each of the five biasing levels. Again, the referenced signal floor is none other than the noise floor for each biased device plot. A strong vertical field sweeps holes to the hole-gas sheet charge near the forward biased junction electrode. Closer to the reverse biased junction electrode, the EBIC signal decreases to levels similar to that of the undoped device's depletion region. According to the simulation plot, the vertical field has reverse polarity compared to that shown in Figure 5-9. This where a horizontal field is formed, similar to the forward biased junction electrode in the undoped device, and sweeps charge carriers at a limiting drift velocity yielding a lower EBIC signal. This explains the obvious decline in the 2DHG device EBIC signal in Figure 5-11 in route toward the reverse biased junction electrode.

As EBIC imaging contrast varies, EBIC signaling is reduced due to the recombination of electron-hole pairs; spatial resolution of device profiling using responsive EBIC signaling is effective in locations where strong recombination centers do not exist but more responsive where they do exist.

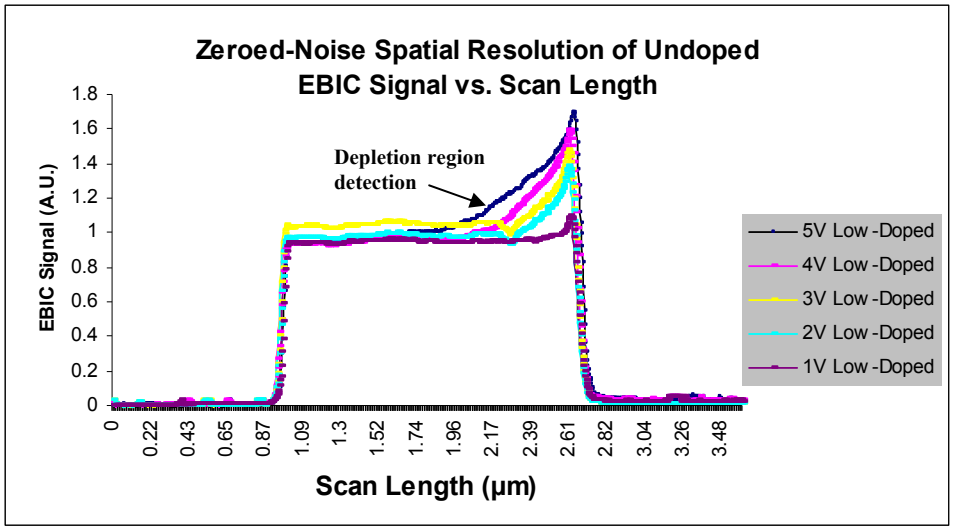

Figure 5-10: EBIC Signal-to-noise profiles of biased undoped HMSM (data used to generate plot courtesy of CNR\IMM, Lecce, Italy)

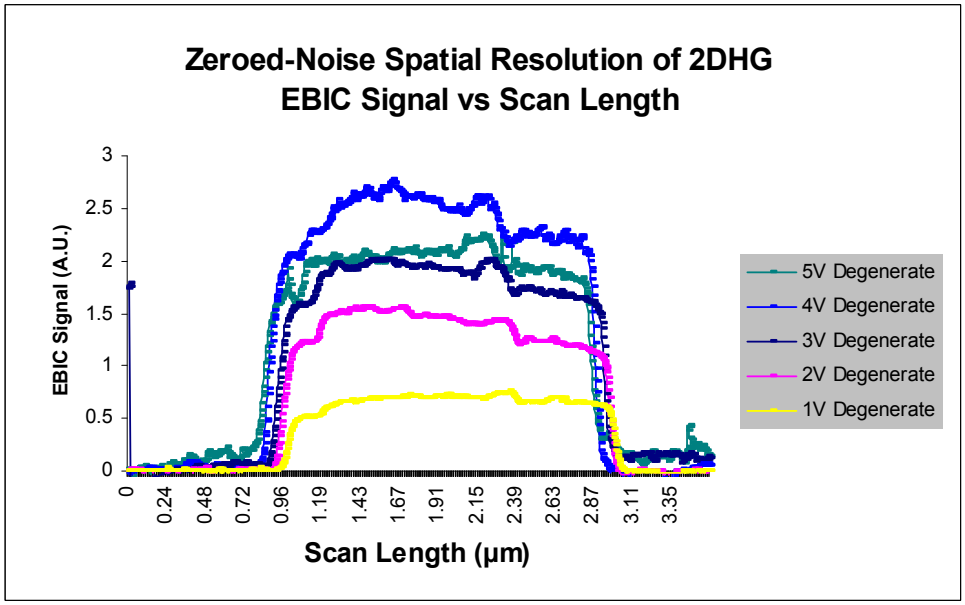

Figure 5-11: EBIC signal-to-noise profiles of biased 2DHG HMSM device (data used to generate plot courtesy of CNR\IMM, Lecce, Italy)

In agreement with the EBIC scan-line profiles of the degenerate HMSM device illustrated in Figure 5-11, previous simulations predicted the electron-hole pairs

generated directly beneath the two-dimensional sheet would be separated, swept, collected by the vertical electric field and detected by the two-dimensional sheet charge. In 2DHG devices, holes are swept to the hole-gas sheet charge and are readily detected by an external EBIC measurement system. However the electrons are swept to the bottom of the device; similar to an undoped device. It is concluded that the EBIC signal for degenerate HMSM devices does not suffer from the horizontal carrier drift limitations found in the GaAs active region of non-degenerate devices.

With an inherently non-existent limiting drift current opposite its depletion region, and observing the proportional increase in highest peak EBIC signal values with an increase in external biasing, the existence of a two-dimensional sheet charge can be proven to reside within a degenerate HMSM device using the EBIC method. If used as a non-destructive tool to identify internal defects for a device, EBIC image contrast variations can aide in identifying device defect locations with a two-dimensional electric-field structure mapping of the device. With proper beam energy control, further study into electron-beam penetration depth perception can add another dimension to internal field mapping for the device.

Characteristic of biased degenerate 2DEG HMSM device simulation, the vertical electric field near the forward biased junction electrode transitions to a horizontal electric field deep into the active region but not as gradual as the vertical field near the reverse biased junction electrode; the electric field orientation transition is more obvious near the reverse biased junction electrode.

Similar to its non-degenerate counterpart, electron-hole pairs collected in the 2DHG device experience a horizontally sweeping electric field near the reverse biased

junction electrode. With the vertical file no longer sweeping charge carriers to the sheet charge, EBIC signaling is lower near the reverse biased junction electrode. Note that the scan-line plots in Figure 5-11 does not possess the limiting drift current near the forward biased junction electrode which is more evident in the undoped device's scan-line plots in Figure 5-10.

6. Conclusion

Based on vertical potential field orientation in the active region for two dimensional charge reservoir detection, the sub-surface potential field variations was used to determine the existence of a two-dimensional charge reservoir. The EBIC signal appeared to be proportional to biasing across entire active region. Device scan-line plot comparison at different biasing levels is more ideal than EBIC image comparison to determine sheet charge existence. Also, the spatial variation dependence on depletion region for the undoped device is observed.

The EBIC method was applied to doped and undoped HMSM structures to probe sub-surface potential-field regions and the electrical differences in the experimental EBIC results were compared. The existence of the two-dimensional charge reservoir modifies the device potential field profile; no spatial potential field variation is evident. There is also higher charge carrier detection in active region for the doped device. With spatial field variations, the depletion region in the undoped structure is detected. The simulation predictions of the doped and undoped sub-surface potential field profiles are experimentally valid.

Contribution to this research study is proving sub-surface potential field variations can be used to determine the existence of a two-dimensional charge reservoir and the importance of the EBIC method in two-dimensional charge reservoir detection.

List of References

[1] $Al_xGa_{1-x}As$. "*Electrical properties - basic parameters.*" Data retrieved (April 2006) from http://www.ioffe.ru/SVA/NSM/Semicond/AlGaAs/ebasic.html.

[2] Bertuccio and Maiocchi. Electron-hole pair generation energy in gallium arsenide by x and γ photons. Journal of Applied Physics, Vol. 92, No. 3, August 2002.

[3] Better Electron Microscopes. "*Is there no way to make the electron microscope better*?" Image retrieved (November 2005) from http://www.rpi.edu/dept/materials/COURSES/NANO/shaw/Page5.html.

[4] Buhmann, Pedrel, Molenkamp, Gurzhi, Kopeliovich, Kalinenko, and Yanovsky. Spectroscopy of electron-electron scattering in a 2DEG.

[5] Chen, Chin, Miller, Ma, and Harris (Jr.). MSM-based integrated CMOS wavelength-tunable optical receiver. IEEE Photonics Technology Letters. Vol. 17, No. 6, June 2005.

[6] Chen, Chin, Miller, Ma, and Harris, (Jr.). Novel electrically controlled rapidly wavelength selective photodetection using MSMs. IEEE Photonics Technology Letters. Vol. 11, No. 1, January/February 2005.

[7] Chen, Nabet, Cola, Quaranta, and Currie. An AlGaAs-GaAs-based RCE MSM photodetector with delta modulation doping. IEEE Electron Device Letters 24(5), 312-314 (2003).

[8] Das, Subramaniam, and Melloch. Effects of electron-beam-induced damage on leakage currents I back-gated GaAs/AlGaAs devices. Department of Electrical Engineering, University of Notre Dame, School of Electrical Engineering, Purdue University. Semicond. Sci. Technol. 8 (1993).

[9] Deddis, Seo, and Jokerst. A 3-D bidirectional optical link using a stacked thin-film emitter detector. IEEE Photonics Technology Letters, Vol. 15, No. 3, March 2003.

[10] Dreyhaupt, Winnerl, Dekorsy, and Helm. High-intensity terahertz radiation from a microstructured large-area photoconductor. Forschungszentrum Rossendorf, Institute of Ion Beam Physics and Materials Research, 2005.

[11] Electron Microscopy; Portland University Department of Physics; retrieved (May 2006) from http://physics.pdx.edu/~jiaoj/lect_4_ph_451.pdf.

[12] Elfwing and Mattias. Nanoscale characterisation of barriers to electron conduction in ZnO varistor materials. Comprehensive Summaries of Uppsala Dissertations from the Faculty of Science and Technology 686, 2002.

[13] Fink, Smith, and Braddock. Electron-beam-induced damage study in GaAs-AlGaAs heterostructures as determined by magnetotransport characterization. IEEE Transactions on Electron Devices, Vol. 37, No. 6, June 1990.

[14] Gurzhi, Kopeliovich, Kalinenko, Yanovsky, Bogachek, Landman, Buhmann, and Molenkamp. Relaxation of high energy quasiparticle distributions: Electon-electron scattering in a two dimensional electron gas. The American Physical Society, Physical Review B 68, 165318 (2003).

[15] Gurzhi, Kopeliovich, and Kalinenko. Electron-electron collisions and a new hydrodynamic effect in two-dimensional electron gas. B. Verkin Institute for Low Temperature Physics and Engineering, National Academy of Sciences of the Ukraine, 310164 Kharkov, Ukraine, (1994).

[16] Gurzhi, Kopeliovich, and Kalinenko. The theory of kinetic effects in two-dimensional degenerate gas of colliding electrons. B. Verkin Institute for Low Temperature Physics and Engineering, National Academy of Sciences of the Ukraine, 310164 Kharkov, Ukraine, (1997).

[17] Hall and Lloyd; The SEM examination of geological samples with a semiconductor back-scattered electron detector; University of Birmingham; retrieved from http://www.geo.arizona.edu/AMS/pdf/am/vol66/AM66_362.pdf.

[18] Hasegawa, Hashizume, Okada, and Jinushi. Fabrication and characterization of quantum wire transistors with Schottky in-plane gates formed by an in situ electrochemical process. Research Center for Interface Quantum Electronics and Graduate School of Electronics and Information Engineering, Hokkaido University, Sapparo 060, Japan. J. Vac. Sci. Technol. B 13(4), Jul/Aug 1995.

[19] He, Hseuh, Gassner, Gullotta, Trbojevic, and Zhang. Calibration of RHIC electron detectors**.** Volume 2, 12-16 May 2003 Page(s):1425 - 1427 Vol.2 . Collider-Accelerator Department, BNL, Upton, NY 11973, USA. Digital Object Identifier 10.1109/PAC.2003.1289727.

[20] Hwang, DeChiaro, Wang, Lin, Zah, Ovadia, and Lee. High-voltage electron-beam-induced-current imaging of microdefects in laser diodes and MESFETs. Bellcore, 33 1 Newman Springs Road, Red Bank, NJ 07701, USA. 1994 IEEE/JIRPS.

[21] Kasai, Hashizume, and Hasegawa. Electron beam induced current characterization of novel GaAs quantum nanostructres based on potential modulation of two-dimensional electron gas by Schottky in-plane gates. Research Center for Interface Quantum Electronics and Graduate School of Electronics and Information Engineering, Hokkaido University, Sapparo 060, Japan. Jpn. J. Appl. Phys. Vol. 35 (1996) Pt. 1, No. 12B.

[22] Leroy. Imaging Coherent Electron Flow Through Semiconductor Nanostructures. Ph.D. Thesis, Harvard University (2001).

[23] Maher and Rossouw. Design and performance of an amplifier for EBIC imaging in a scanning electron microscope. J. Phys. E / Sci. Instrum.. Vol. 16. 1983.

[24] Marso, Wolter, and Kordos. A novel two-color photodetector based on an InAlAs–InGaAs HEMT layer structure. IEEE Photonics Technology Letters, Vol. 16, No. 11, November 2004.

[25] Mir, Bateman, Connolly, Derbyshire, Duxbury, Lipp, Simmons, Spill, and Stephenson. Studies of the gain properties of gas microstrip detectors relevant to their application as X-ray and electron detectors. Nuclear Science Symposium Conference Record, 2001 IEEE. Volume 1, 4-10 Nov. 2001 Page(s):306 - 310 vol.1.

[26] Muller and Kamins. Device electronics for integrated circuits, second edition. Wiley & Sons, 1986.

[27] Neamen. Semiconductor physics and devices, third edition. McGraw-Hill Science/Engineering/Math; 3 edition (August 22, 2002).

[28] Nikolaev, Melnik, Blashenkov, Kuznetsov, Nikitina, Zubrilov, and Tsvetkov. GaN layers grown by HVPE on p-type 6H-SiC substrates. Internet Journal of Nitride Semiconductor Research, Vol. 1, Article 45; retrieved from http://nsr.mij.mrs.org/1/45/complete.html.

[29] Pedrel, Buhmann, Molenkamp, Gurzhi, Kopeliovich, Kalinenko, Yanovsky, Bogachek, and Landman. Effects of electron-electron scattering of electron-beam propagation in a two-dimensional electron-gas. The American Physical Society, Physical Review B 62, No. 3, July (2000).

[30] Ragi, Romero, and Nabet. Modeling the electrical characteristics of Schottky contacts in low-dimensional heterostructure devices. IEEE Transactions on Electron Devices, Vol. 52, No. 2, February 2005.

[31] Rajopadhye, Singh, Raja, and Khokle. SEM-EBIC studies of electron beam irradiation memory effects in a-Si : H. IEE Proceedings, Vol. 135, Pt. I , No. 5, October 1988.

[32] Rhoderick and Williams. Metal-semiconductor contacts. Clarendon (Oxford) Publishing (1988).

[33] Ruff, Aliberti, Giza, Shen, Stann, and Stead. Characterization of a 1x32 element metal–semiconductor–metal optoelectronic mixer array for FM/cw LADAR. IEEE Sensors Journal, Vol. 5, No. 3, June 2005.

[34] Scanning Electron Microscope and Microprobe; Department of Civil and Environmental Engineering, Stanford University; retrieved from eep.stanford.edu/seepweb/cee373/lect9.pdf.

[35] SEM Component Details (2003); Department of Chemical Engineering and Materials Science; Michigan State University; retrieved from http://www.chems.msu.edu/curr.stud/mse.sops/sem.det.htm.

[36] SEM: Imaging with Secondary Electrons Comparison of Detectors (2004); Eidgenössische Technische Hochschule Zürich; retrieved from http://www.microscopy.ethz.ch/se-detectors.htm.

[37] Siliconfareast.com; Electron Beam-Induced Current (EBIC) Analysis; retrieved from http://www.siliconfareast.com/ebic.htm.

[38] Song, Seo, Hyun, Kim, Huang, Brooke, Jokerst, and Brown. A 10 Gbit/s Si CMOS trans-impedance amplifier with an integrated MSM photodetector for optical interconnections. Georgia Institute of Technology, 2004.

[39] Suzuki, Nonaka, Ogawa, Cho, Seo, and Jokerst. Embedded optical interconnections on printed wiring boards. Packaging Research Center, Georgia institute of Technology, 2004.

[40] Sze. Physics of semiconductor devices, second edition. Wiley & Sons, 1981.

[41] Thomann and Ralf (2001); EDX : Energy Dispersive X-ray Analysis; (elemental analysis); University of Freiburg; retrieved from http://www.polymermicroscopy.com/edxeng.htm.

[42] Topinka, LeRoy, Westervelt, Maranowski, and Gossard. Imaging coherent electron wave flow in a two-dimensional electron gas. Physica E 12 (2002) 678 – 683.

[43] Yanovsky, Predel, Buhmann, Gurzhi, Kalinenko, Kopeliovich, and Molenkamp. Angle-resolved spectroscopy of electron-electron scattering in a 2D system. ARXIV Mesoscopic Systems and Quantum Hall Effect (2000), University Wuerzburg, Germany, and B. Verkin Institute for Low Temperature Physics & Engineering, Kharkov, Ukraine), bibl. Code: 2000cond.mat..9005Y.

[44] Yost, Madjar, and Herczfeld. Frequency response mechanisms for the GaAs MSM photodetector and electron detector**.** IEEE Transactions on Microwave Theory and Techniques, Vol. 49, No. 10, Oct. 2001.

[45] Zhao. Carrier transport in high-speed photodetectors based on two-dimensional-gas. PhD thesis, Photonics, Drexel University (2006).

Appendix A: EBIC Amplifier Circuit Design

With the design of the EBIC circuit in Figure A-2, a compromise between noise and sensitivity had to be fully considered with the major contributor of the noise levels at the EBIC amplifier's output being the amplifier itself. With a simulated amplifier gain of 3 x 10^9 V/A, EBIC image degradation may be introduced when operated at maximum sensitivity. As an added circuit design feature, a 12 kHz filter is introduced to reduce high frequency noise when the SEM's slow-scan mode is in use [23].

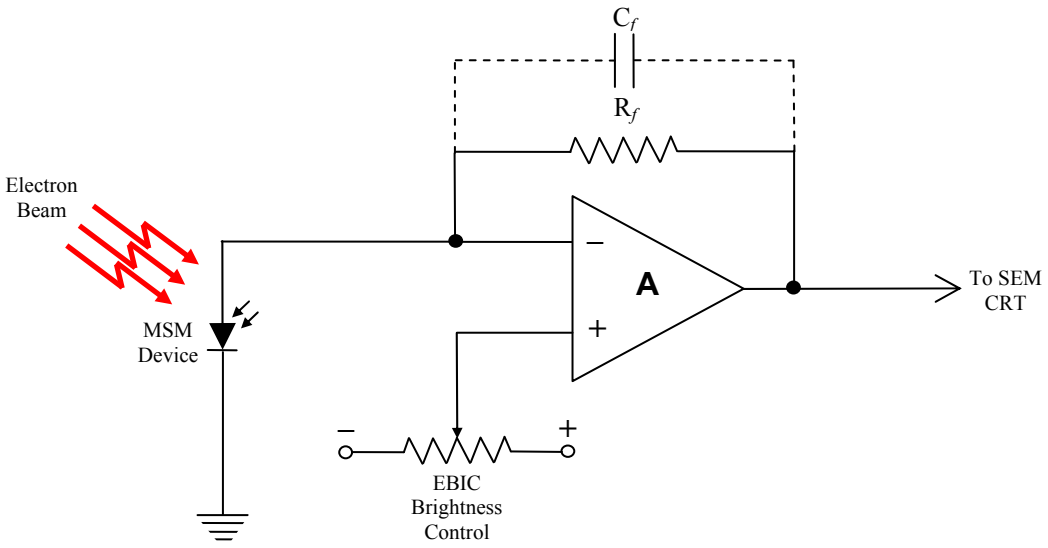

Figure A-1: Overall EBIC amplifier circuit [23]

In chronological order of input-to-output staging, the 5-stage EBIC circuit includes a trans-impedance amplifier stage, an optioned phase-reversal/low-pass filter stage, two variable-gain stages, and a voltage-follower or buffer stage. With unity-gain

at the buffer stage, the overall system gain can be represented with the following equation:

$$V_{Out} = \mathbf{A} \cdot I_{EBIC} = (A_{Trans} \cdot A_{Ph\_Rev} \cdot A_{Gain1} \cdot A_{Gain2} \cdot A_{Unity}) \cdot I_{EBIC} \qquad (21)$$

To avoid any added cabling noise or capacitance to the low-level signal, it is advantageous to the PCB designer to build the SEM sample holder with the complete circuit in Figure A-2, or at least the trans-impedance input stage, directly on the holder. The phase-reversed/12 KHz filter stage (S_1 & S_2) provides the ability to invert image contrast by inverting the input signal's polarity. By changing the feedback resistance of the variable gain stages (S_3 & S_4), the amplification of the two-stage gain can range from 10^0 V/V to 10^4 V/V. At maximum sensitivity ($|A| = 3 \times 10^9$ V/A) with the 12 kHz filter bypassed and the phase reverse stage inactive, the trans-impedance amplifier has a 70.7% max gain roll-off @ 600 kHz (see Figure A-6). As its name suggests, the unity buffer stage is self-explanatory. The brightness control potentiometer shown in Figure 3-1 represents the offset-voltage control which can be used to modify image intensity.

With various scan rates available, the design of an EBIC system would have to accommodate the dwell-time speeds of the pre-existing SEM imaging system. For most SEM imaging systems, a 600 kHz bandwidth circuit would allow adequate EBIC imaging with fast data acquisition of about 2 full frames per second (approximately 3.35×10^5 scan points). Requirements for today's television input signal scan rate include a 4 MHz bandwidth minimum, therefore, the EBIC circuit is designed specifically for the useful bandwidth of SEM monitors which handles bandwidths in the

200 kHz range. Slower scan-rate imaging resolution, which can be as low as 50 seconds per frame, can be improved by utilizing the 12 kHz filter at the phase-reversal stage (S_2) [23].

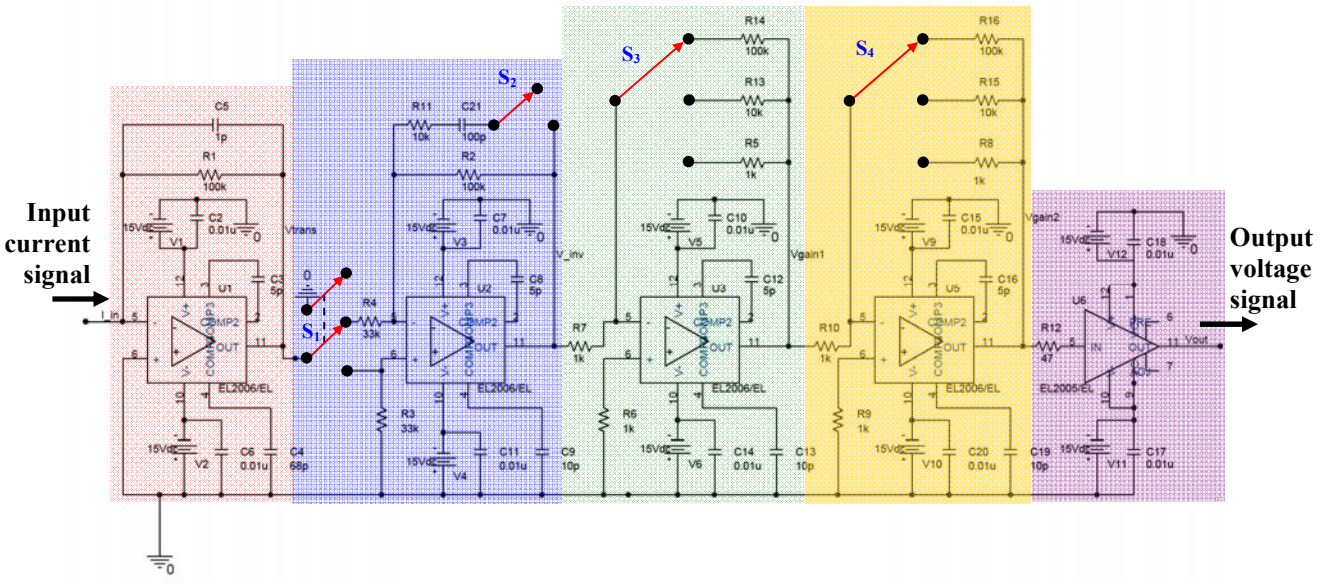

Figure A-2: Component level of trans-impedance EBIC circuit design

The test device used for simulation included an input current source range of 300pA to 10uA, a 50pF capacitor and a 10MΩ resistor all in a parallel 3-branch configuration which is typical for photo-detection simulation. All of the operational amplifiers used in the design are manufactured by Elantec Semiconductor; four of the five stages use the EL2006 amplifier and the fifth using the EL2005 buffer amplifier.

Simulation results for the EBIC circuit design show promising circuit characteristics which include EBIC signal detection as low as 300 pA, a high level of user-control, and very high trans-impedance gain (10^5 V/A). At minimum sensitivity

($A_{gain1} = A_{gain2} = 10^0$ V/V) the transimpedance amplifier gain has a 3 x 10^5 V/A per decade roll-off just above 1.0 MHz (in-phase signaling). At maximum sensitivity ($A_{gain1} = A_{gain2} = 10^4$ V/V) the transimpedance amplifier gain has a 3 x 10^9 V/A per decade roll-off just below 600 kHz (in-phase signaling). Thus the maximum signal gain will come at a cost of approximately 400 kHz of bandwidth. With EBIC currents in the pico-amp/micro-amp range, the overall ideal output of the amplifier circuit can be controlled to sweep rail potentials from -4V to 4V (or -3V to 3V) which is enough to drive an existing SEM monitor's pixel through its full contrast range [23].

Note that the simulated EBIC circuit design does not include any test device biasing or any reference to the DC-offset control circuitry for the amplifier stages. Implementation of the DC-biasing and DC-offset circuitry will change the electrical response properties of the amplifier circuit design. By reducing the variable gain stages' amplification to 10^0 V\V, input currents as high as 10μA can output the needed ±3V or ±4V swing for SEM monitoring.

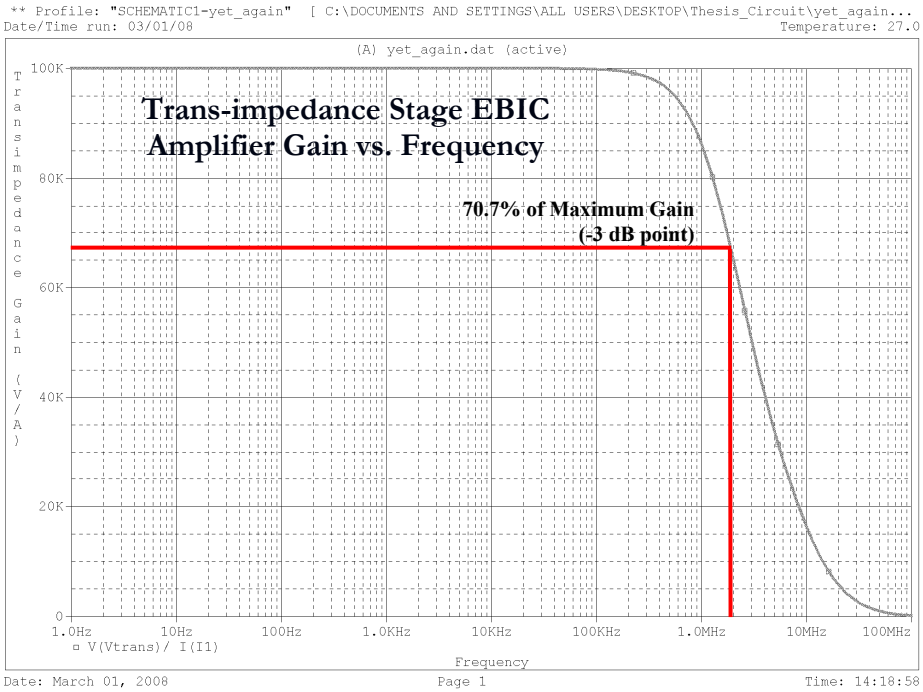

Figure A-3: Trans-impedance stage gain versus frequency

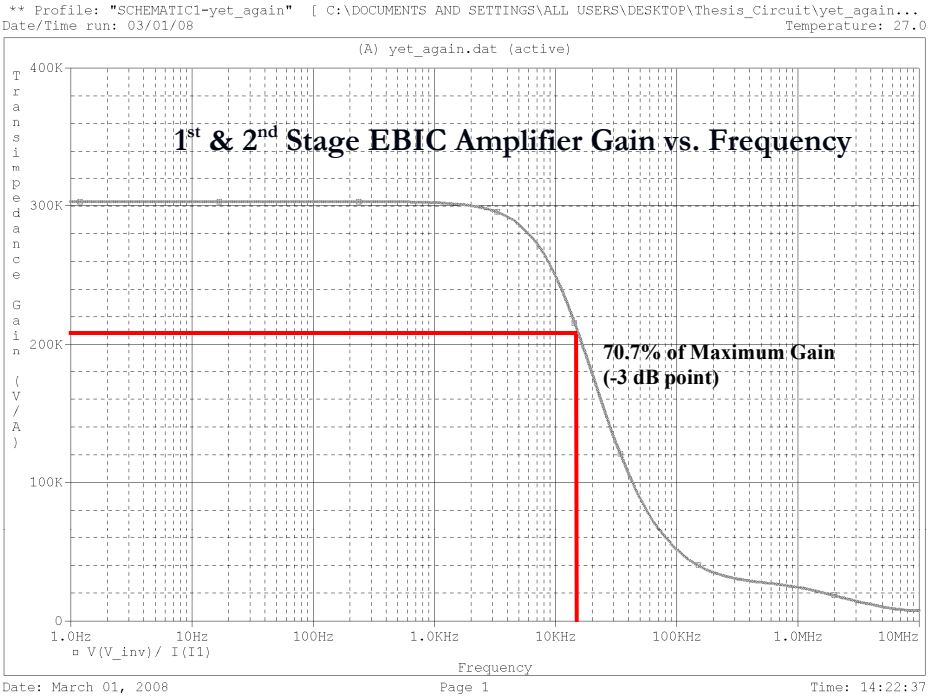

Figure A-4: In-phased gain stage output versus frequency with 12 KHz filter active

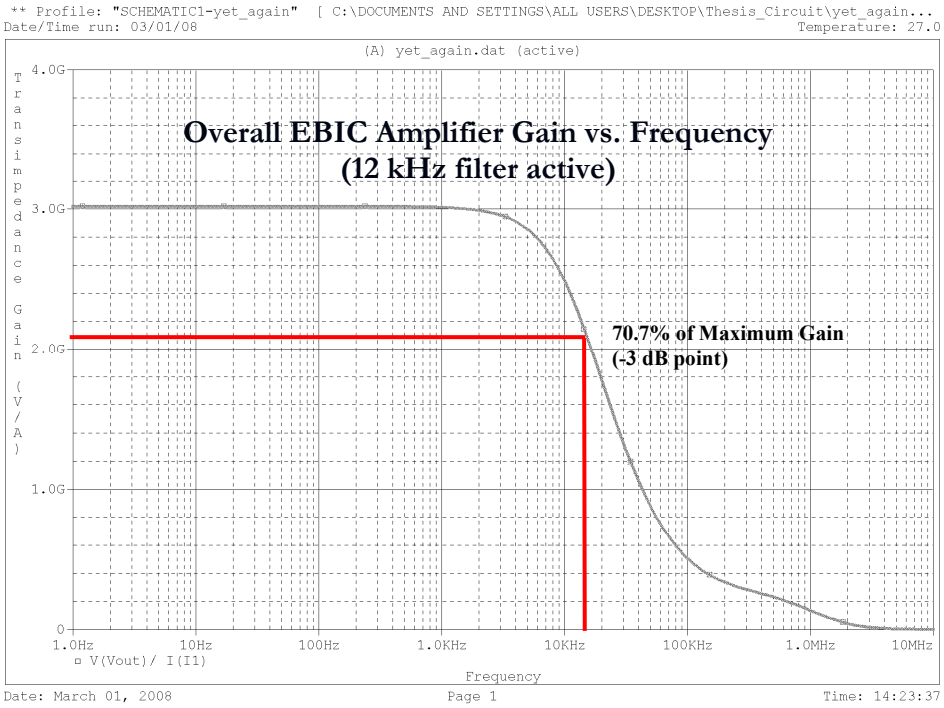

Figure A-5: Overall gain versus frequency with 12 kHz filter active

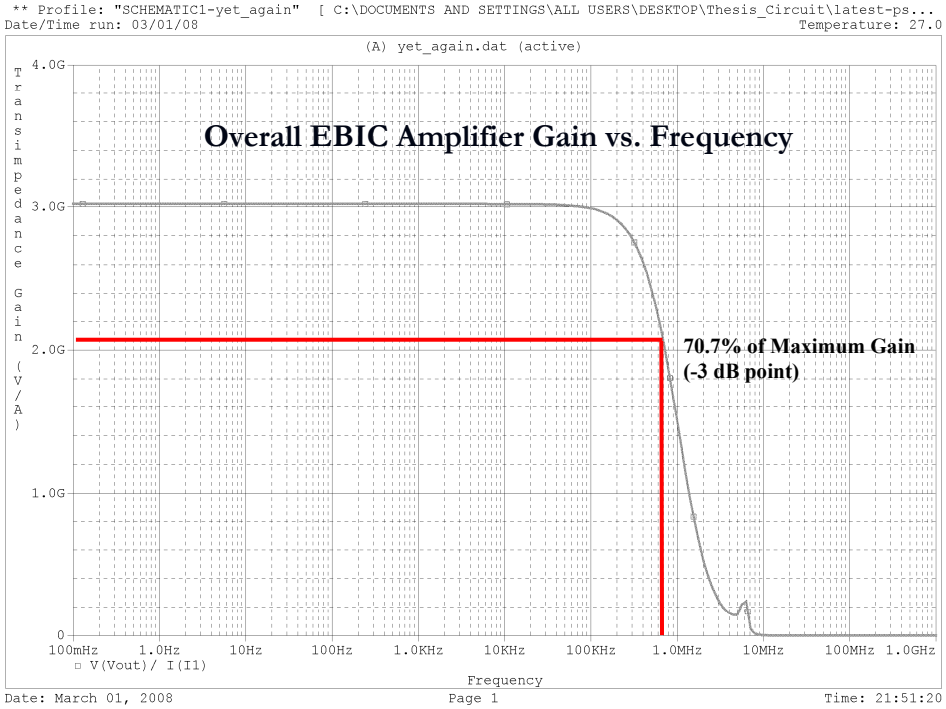

Figure A-6: Overall gain versus frequency with inactive 12 KHz filter

Appendix B: Acronym List

Acronym	Description
2DEG	Two-dimensional electron gas
2DHG	Two-dimensional hole gas
AlGaAs	Aluminum-gallium arsenide
BSE	Backscatter electron
CL	Cathodoluminescence
CRT	Cathode-ray tube
EBIC	Electron beam induced current
EBT	Electron beam tomography
GaAs	Gallium arsenide
HMSM	Hetero-junction metal-semiconductor-metal
I-MSM	Inverted metal-semiconductor-metal
InP	Indium phosphide
IPG	In-plane gate
LED	Light-emitting diode
MS	Metal semiconductor
MSM	Metal-semiconductor-metal
PD	Photo-detector
PIN	P-type, intrinsic, n-type doped structure
PWB	Printed wiring board
SE	Secondary electron
SEM	Scanning electron microscope or scanning electron microscopy
TEM	Transmission electron microscope